UNIVERSIDAD NACIONAL AUTÓNOMA DE MÉXICO

PROGRAMA DE MAESTRÍA Y DOCTORADO EN INGENIERÍA

Theoretical and experimental characterization of wakes generated by localized magnetic forces in electrically conducting fluids.

TESIS

QUE PARA OPTAR POR EL GRADO DE:

DOCTOR EN INGENIERÍA

ENERGÍA - PROCESOS Y USO EFICIENTE DE ENERGÍA

P R E S E N T A:

JOSÉ JOEL ROMÁN GODÍNEZ

DIRECTOR DE TESIS:

DR. SERGIO CUEVAS GARCÍA

INSTITUTO DE ENERGÍAS RENOVABLES

TEMIXCO, MORELOS, AGOSTO,2017

JURADO ASIGNADO:

Presidente: Dr. Eduardo Ramos Mora

Secretario: Dr. Jorge Antonio Rojas Menéndez

Vocal: Dr. Sergio Cuevas García

1er. Suplente: Dr. Alberto Beltrán Morales

2do. Suplente: Dr. Aldo Figueroa Lara

Lugar donde se realizó la tesis:

Instituto de Energías Renovables , Temixco, Morelos, México.

TUTOR DE TESIS:

Dr. Sergio Cuevas García

_____

FIRMA

Contents

Abstract

This thesis is mainly devoted to the experimental and numerical study of wakes generated by localized Lorentz forces, named magnetic obstacles, in both electrolytes and liquid metals. As a complement, some experimental results of wake patterns behind a solid circular disk are also presented. The motivation of the study arises from multiple fluid systems of technological interest, mainly in energy related applications, where the understanding of wake patterns behind obstacles is of prime importance. These include problems of fluid-structure interaction, for instance in wind energy systems, as well as heat transfer enhancement devices. The term magnetic obstacle refers to Lorentz forces created in conducting fluids by the interaction of induced or applied electric currents with localized external magnetic fields. In addition to offering an alternative to the production of wakes in laboratory experiments, flows past magnetic obstacles are of importance in a novel measurement technique called Lorentz force velocimetry. Likewise, these flows may find important applications in heat exchangers. Firstly, the wakes generated in a thin layer of electrolyte by traveling localized Lorentz forces produced by the interaction of an applied electric current and the field of a moving magnet, are analyzed. Flow visualization using dye along with Particle Image Velocimetry (PIV) were used to characterize the flow. Different patterns were identified as well as the transition between them, while the main characteristic features were reproduced through a quasi-two-dimensional (Q2D) numerical model. This model was also used to investigate the wake patterns created by a pair of magnetic obstacles placed side by side in a layer of electrolyte. By varying the separation between the obstacles and the intensity of the applied electric current, the characterization of different flow patterns was carried out. The resemblance with wake patterns reported for a pair of solid obstacles is remarked. Further, with the aim of determining the influence of the confining walls in the flow past a magnetic obstacle, an experimental study was performed where the effect of the blockage parameter, namely the ratio of the characteristic length of the magnet and the separation between the confining lateral walls, was explored. Results allow to build a map of qualitative behavior that characterize the flow patterns for four values of the blockage parameter in terms of the dimensionless governing parameters, namely, the Reynolds number and the Lorentz force parameter. The study was complemented with numerical simulations based on the Q2D model. The present work also comprises the experimental and numerical analysis of the flow past a magnetic obstacle in a liquid metal flow where a localized Lorentz force is created by the interaction of currents induced by the fluid motion and an external magnetic field spot. Experiments were carried out in a liquid metal loop driven by an induction pump while measurements were obtained through Ultrasonic Doppler Ve-

locimetry. The main objective of the analysis was to understand the interplay of inertial, viscous, and magnetic forces and demonstrate that a liquid metal vortex shedding flow can be relaminarized when inertia overcomes the induced magnetic force. Using a Q2D model, numerical simulations allowed to reproduce the main physical features of the flow. Finally, a complementary study on the wake patterns behind a solid circular disk, carried out during an internship at ESPCI, in Paris, France, is presented. The study involved PIV measurements of velocity fields and the analysis of the longitudinal vorticity component using the azimuthal Fourier decomposition technique with the aim at characterizing the three-dimensional wake. The main findings of the present study are summarized in the final conclusions.

Introduction

One of the fundamental problems of fluid dynamics that has occupied scientists and engineers for many years is the flow past solid obstacles. From the basic point of view, this problem poses a multitude of theoretical and experimental challenges since we are dealing with complex dynamical systems with a vast wealth of behavior. Its study has allowed fundamental advances in topics such as boundary layer, instability, chaos and transition to turbulence, and despite the innumerable works reported in the specialized literature, it is currently a relevant topic of research with different variants which are still far from being fully understood. The great interest generated in the study of flows over obstacles comes essentially from their presence in countless technological applications, as well as in various natural phenomena. This problem is also related in many ways to the transport and efficient use of energy. The optimal design of land, air and marine vehicles, for example, requires an accurate knowledge of the behavior of the flows past on these bodies. Equally important are flows driving wind turbines as well as those affecting buildings or other constructions where structural aspects are of vital importance (Irwin, Sept. 2010). Flows past obstacles are widely used in various heat exchangers in order to improve heat transfer by generating vortices. Precisely, what characterizes the flows past obstacles is the formation of wakes behind them, where vortices are generated due to the detachment of the boundary layer initially adhered to the object. The nature of these wakes depends mainly on the Reynolds number and it may exhibit steady or time-dependent behavior and being laminar to turbulent, with a range of behaviors between these regimes(Zdravkovich, 1997). While in certain applications it is desired to suppress or minimize the existence of vortices in the wake behind objects, and thereby the associated energy dissipation e.g., in the design of vehicles (Moin and Kim, January. 1997) in other cases it is intended to generate the largest number of vortices that allow a greater energy transport as in the heat exchangers (Fiebig, 1997). It has also been proposed the use of the Bénard-von Kármán (BvK) wake to capture energy through a membrane placed in a way that interacts with the wake (Allen and Smith, 2001).

Studies have also been carried out on the structures observed in wakes and the flow patterns that are formed when flows interact with solid obstacles or oscillating aerodynamic profiles. For instance, Godoy-Diana et al. (2008) analyzed a flow governed by three dimensionless parameters, the Reynolds number, the amplitude of a flapping aerodynamic profile and the frequency of oscillation. They found three flow patterns, namely, the Bénard-von Kármán street (BvK), alignment of vortices on a central axis and the reverse Benárd-von Kármán street (rBvK). In the latter the direction of rotation of each vortex is

reversed with respect to the classical BvK-wake. In addition to these three flow patterns there is a wide variety of wakes found behind a foil, some of them are the 2P wake (which will be described later), the 2P+2S wake and a variety of wakes with up to 16 vortices per oscillation period (Schnipper et al., 2009). As well as the oscillation of the solid obstacle produces intriguing wake modifications, very interesting patterns are observed when the wakes created by different obstacles interact (Peschard and Le Gal, 1996). In fact, the flow patterns found behind a pair of solid obstacles depend, in addition to the Reynolds number, on the proximity between them. It has been reported in experimental and theoretical studies that a bistable flow pattern appears for certain values of the separation between the solid obstacles(Zdravkovich, 1985; Le Gal et al., 1990; Peschard and Le Gal, 1996; Sumner et al., 1999). Another interesting question is how the wake behind solid obstacles is modified when the wake interacts with a solid wall instead of another solid obstacle. In fact, the flow pattern presents a steady behavior at higher Reynolds numbers than those found in the unbounded case (Davis et al., 1984; Camarri and Giannetti, 2007; Singha and Sinhamahapatra, 2010). The wakes previously mentioned such as the BvK wake, the rBvK wake, the 2P wake and some others are examples of wakes in two dimensional systems. Evidently, there are many flows past solid obstacles where three dimensional effects are very important, for example in flows past a sphere, a disk or a cube. It has been found that behind these three bodies appears the same transition flow pattern as a function of the Reynolds number. At low Reynolds numbers, the first observed flow pattern is an axisymmetric flow; by increasing the Reynolds number two counter-rotating vortices appears and finally, for a high Reynolds number, the Hairpin vortex is found (Gumowski et al., 2008; Bobinski et al., 2014; Klotz et al., 2014).

The interaction of viscous flows with solid obstacles is not the only way to create wake patterns. In fact, localized electromagnetic forces generated by the interaction of an external magnetic field with an applied or induced electrical current in an electrically conductive fluid may act, under some conditions, as an obstacle for the fluid and reproduce flow patterns observed behind solid obstacles although more complex patterns can also arise. (Cuevas et al., 2006a; Afanasyev and Korabel, 2006b; Votyakov et al., 2007). Despite the similarity between flows past a solid obstacle and flows generated by the action of a localized electromagnetic force, it is recognized that there are important differences between them (Votyakov and Kassinos, 2009, 2010). Differences are originated owing to the fact that while flows past solid obstacles are governed by a single parameter, namely, the Reynolds number, flows interacting with a localized electromagnetic force involve a second governing parameter: the Hartmann number. This parameter estimates the importance of magnetic forces compared with viscous forces and it is usually larger in a liquid metal due to its high electrical conductivity. The existence of a second governing parameter may lead to flow behaviors very different from those observed in the flow past solid obstacles. In the case of liquid metal flows, the relative motion between the fluid and the applied magnetic field induces electric currents that interact with the magnetic field and generate a localized Lorentz force that points in opposite direction to the fluid motion, acting as an obstacle. (Cuevas et al., 2006a,b; Votyakov et al., 2007, 2008; Domínguez et al., 2015). For this reason, Cuevas et al. (2006b) coined the term *magnetic obstacle* to refer to a localized Lorentz force that opposes the flow. Several theoretical and experimental studies

have been developed on the flow past a magnetic obstacle (Votyakov et al., 2008; Kenjeres et al., 2011; Tympel et al., 2013; Domínguez et al., 2015). The presence of several magnetic obstacles on the flow has been addressed numerically by Kenjeres (2012) and the possibility of using arrangements of magnetic obstacles for heat transfer enhancement has also been explored (Zhang and Huang, 2013).

Owing to the low electrical conductivity of electrolytes, induced currents are negligible and do not produce a noticeable localized Lorentz force. However, a Lorentz force can be created in electrolytes by applying an external electric current which interacts with the applied magnetic field (Honji, 1991; Honji and Haraguchi, 1995; Afanasyev and Korabel, 2006b). Some experimental (Honji, 1991; Honji and Haraguchi, 1995; Afanasyev and Korabel, 2006b; Alcalá and Cuevas, 2014; Román et al., 2017) and numerical studies (Beltrán, 2010; Román et al., 2015) have explored these flows, however they are quite few compared to those involving liquid metals. It has been observed that for a fixed electromagnetic force strength, the transition flow pattern in an electrolyte as the Reynolds number increases presents a jet-like flow, a traveling dipole vortex and vortex shedding (Román et al., 2017; Honji and Haraguchi, 1995; Afanasyev and Korabel, 2006b). The experimental configuration used in the electrolyte studies mentioned above, consists of a rectangular container with a layer of electrolyte where electrodes are placed along the larger side of the container so that an external electric current can be applied transversally while a permanent magnet is moved with a constant velocity underneath the container perpendicularly to the applied current. A similar experimental configuration, although without applied currents, has been also used to study vortex patterns in liquid metal flows (Samsami et al., 2014; Prinz et al., 2016).

The main purpose of the present work is to contribute, through experimental studies and numerical simulations, to the understanding of the dynamics of flows past magnetic obstacles. This work comprises both, the study of the wake generated behind a magnetic obstacle in a thin layer of electrolyte under different configurations and the study of the wake generated behind a magnetic obstacle in a liquid metal duct flow. In addition, a brief study of the wake behind a solid obstacle, which was performed during a stay at the École Suppérieure de Physique et de Chimie Industrielles de la Ville de Paris (ESPCI-ParisTech), is included. Apart from the present introduction, the thesis contains five additional chapters.

In Chapter 1, the wake patterns behind a magnetic obstacle in an electrolyte layer are studied. Flows are analyzed qualitatively by visualization from above using dye, and through PIV measurements of velocity fields and vorticity distribution. Vorticity fields as a function of time show the transition between Bénard-von Kármán wake (BvK wake) and a 2P wake. It is important to remark that this transition in the flow behind a magnetic obstacle in an electrolyte layer has not been reported in previous studies. The experimental results are condensed in an experimental flow transition map. A quasi-two dimensional (Q2D) numerical model is used to reproduce the experimental observations. Numerical and experimental results confirm that, under certain parameter values, inertia overcomes the electromagnetic braking force.

Chapter 2 is mainly focused on the numerical analysis of the flow past a pair of magnetic obstacles, placed in side by side configuration, in an electrolyte layer. The flow is simulated using a Q2D numerical model. The flow is analyzed for different values of the separation distance between the magnetic obstacles for a fixed Reynolds number. Through numerical Lagrangian tracking and Fourier analysis, the characteristic regimes of the flow are identified and compared with those observed in flows past a pair of cylinders.

The experimental and theoretical study of the interaction between the wake behind a magnetic obstacle and the lateral walls is presented in Chapter 3. The effect of the walls in the flow patterns is explored through the variation of the blockage parameter, β, which is the ratio between the length of the magnet and the width of the channel in the cross stream direction. As the blockage parameter varies the flow patterns are analyzed by visualization of the flow using dye and simulated numerically using a Q2D model. Transition flow maps are obtained as a function of the Reynolds number and Lorentz force parameter for the four values of the blockage parameter explored. Numerical simulations reproduce the flow behavior and the transition flow maps and allow the identification of two flow patterns that have not been reported in the literature.

In Chapter 4, an experimental study of the flow past a magnetic obstacle in liquid metal duct flow is presented. The liquid metal (GaInSn eutectic alloy) circulated in a loop driven by an induction electromagnetic pump along the channel length. Experimental measurements of the u component of the velocity are made with an Ultrasonic Doppler Velocimeter (UDV). These measurements show a transition from steady state to a time-dependent flow as the Reynolds number increases, but if this number continues to grow, the steady flow is again recovered. The Q2D numerical model captures the main physical flow behavior and reproduces the experimental results satisfactorily.

In Chapter 5, as a complement to the study of wakes, the flow past a solid circular disk immersed in a water channel is presented. The flow is explored experimentally in a plane normal to the flow direction. The temporal evolution of the longitudinal component of vorticity is analyzed using azimuthal Fourier decomposition with the aim at understanding different wake patterns.

Finally, we present the main conclusions of this thesis.

Experimental and numerical study of wake patterns behind a magnetic obstacle in an electrolyte layer

In this Chapter[1], we present an experimental and numerical study of vortex wakes produced by a travelling localized Lorentz force in a thin layer of electrolyte. The fluid is contained in an open rectangular channel with two parallel electrodes placed along the longest walls so that a uniform DC current is supplied through the layer. A permanent magnet located underneath the container is moved with a constant velocity so that the interplay of the moving magnetic field and the applied transversal current generates a Lorentz force. The variation of the applied current and the velocity of the magnet leads to different vortex patterns such as jet-like flow, travelling vortex dipole, Bénard-von Kármán wake and 2P wake, which are visualized with tracers and analyzed using Particle Image Velocimetry. The flow is governed by the Reynolds number, based on the velocity and size of the travelling magnet, and the Chandrasekhar number, based on the applied current. An experimental map characterizing different flow patterns and the transition among them is built in terms of these parameters. Numerical results using a quasi-two-dimensional model reproduce the main features observed in the experiments.

1.1   Introduction

The study of vortex formation and evolution in wakes is of prime importance for countless applications and natural phenomena involving fluid-structure interactions. For instance, the mechanisms underlying different propulsion strategies in animals and man-made devices or those that allow to optimize equipments for heat transfer enhancement, rely on a deep understanding of the spatio-temporal behavior of wakes.

There is a wide variety of wakes reported in the literature of the flow past solid obstacles. The best known is the classical Bénard-von Kármán (BvK) wake observed when a free stream impinges on a fixed cylinder (Zdravkovich, 1997). This represents a drag wake and is probably the most studied due to its ubiquity in many applications. In the reverse

---

[1]This Chapter is mainly based on the paper: Román, J., Figueroa A. Cuevas, S., 2017, "Wake patterns behind a magnetic obstacle in an electrolyte layer". *Magnetohydrodinamics*, **53**, 55 - 66.

Bénard-von Kármán (rBvK) wake the direction of rotation of each vortex is reversed with respect to the classical BvK wake and is a feature of propulsive motion (Godoy-Diana et al., 2008). Another wake that occurs behind oscillating structures such as cylinders and aerofoils is the 2P wake where two vortex pairs are shed per oscillation period (Schnipper et al., 2009). Interestingly, experimental studies have reported the transition from a one kind of wake to another (Godoy-Diana et al., 2008).

Magnetohydrodynamic flows offer an alternative for the generation of wakes in electrically conducting liquids in the absence of solid bodies. In fact, it has been shown that localized Lorentz forces act as obstacles for the flow and produce vortex patterns that resemble, in some aspects, the flows past solid obstacles (Cuevas et al., 2006a; Afanasyev and Korabel, 2006b; Votyakov et al., 2007). When the conducting fluid is a liquid metal, the relative motion of the fluid and a localized field induces electric currents that interact with the same field to produce a Lorentz force that oppose the liquid (Cuevas et al., 2006a; Votyakov et al., 2007, 2008; Domínguez et al., 2015). Although some vortex patterns are observed in either electrolytes or liquid metals, some others like the six-vortex pattern are distinctive features of liquid metal flows under specified conditions (Votyakov et al., 2007). A variety of characteristic phenomena like the formation or suppression of vortices, symmetry breakdown, and vortex shedding has been observed in flows driven in a liquid metal layer by an external magnet in rectilinear motion (Samsami et al., 2014; Prinz et al., 2016).

Wakes produced by localized electromagnetic forces in electrolytes have been less studied than those in liquid metals. The few experimental studies reported in the literature used similar setups in which a shallow layer of electrolyte is contained in a long open rectangular channel, while a DC current is applied transversally to the long axis of the channel. A permanent magnet located either upon or beneath the channel is moved at a constant velocity along the center line of the container so that a travelling localized Lorentz force is produced. In this way, using a single moving magnet Honji (1991) and Honji and Haraguchi (1995) visualized different flow patterns such as vortex dipoles, vortex shedding and a wavy wake. In turn, Afanasyev and Korabel (2006b) considered flows produced by a single magnet as well as by two magnets with opposite orientations, aligned with the direction of motion and separated by a short distance. They observed travelling dipoles as well as stable and unstable wakes. Another experimental study by Alcalá and Cuevas (2014) found that when the velocity of the magnet surpass a threshold, the Lorentz force is able to generate a stationary wave pattern on the free surface. Finally, Román et al. (2015) explored numerically the flow past a pair of magnetic obstacles side by side and made a comparison of the flow regimes with those corresponding to the flow past solid cylinders.

In this work, we use an experimental set up similar to the one described above to explore different flow patterns generated by a travelling localized Lorentz force in a shallow electrolyte layer. We take advantage of the transparency of the electrolyte to characterize the flows through tracer visualization and Particle Image Velocimetry (PIV) measurements. In particular, the study is focused on the analysis of the observed flow transitions which

occur as the control parameters are varied. The study is complemented with numerical simulations based on a quasi-two-dimensional numerical model.
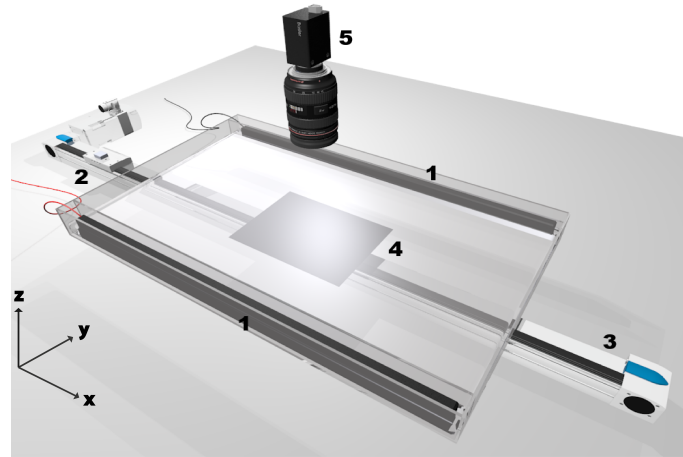
1.2   Experimental set up

Figure 1.1: Experimental setup. A localized Lorentz force is created by a DC current applied through parallel electrodes (1) and the field of a permanent magnet (2) moved beneath the container with a linear actuator (3). The flow is studied at the observation zone (4) with the aid of a camera (5), using dye visualization and PIV method.

The experimental set-up consists of an acrylic channel 100 cm long, 40 cm width, and 10 cm height. Two electrodes (square graphite rods of 1 cm^2 of cross-section and 80 cm long) were placed along the two long sides of the container and connected to a power supply that provided a DC current from 0.5 to 5 A. Electrodes were located inside chambers (bubble traps) that allow the electric current to flow at the bottom while preventing the bubbles to invade the main flow region. The channel is partially filled with a weak electrolytic solution of sodium bicarbonate ($NaHCO_3$) at 8.6% by weight, forming a layer of 3 mm deep. The mass density, kinematic viscosity and electrical conductivity of the electrolyte are $\rho = 1.09 \times 10^3$ Kg/m^3, $\nu = 10^{-6}$ m^2/s and $\sigma = 6.36$ S/m, respectively. The channel is mounted on four supports and leveled up to get a horizontal layer of water solution with uniform thickness. A square neodymium magnet with side length of 2.54 cm, height of 1.27 cm, and maximum magnetic strength on its surface of 0.33 T is placed underneath the bottom wall of the channel and moved along its symmetry axis with a constant velocity using a linear actuator (FESTO EGC-70-500-TB-KF- 0H-GK) driven by a servo motor (FESTO EMMS-AS-70-M-RS) (see Figure 1.1). The interaction of the DC current with the field of the moving magnet generates a travelling Lorentz force that creates a flow pattern on the electrolyte. The flow was visualized from the top using dye as tracer and pictures were taken with a Nikon D80 camera with a AF micro-nikkor 60 mm f/2.8 D lens. In order to ensure the contrast between the dye and the flow, the bottom

wall was covered with a white sheet. In addition, PIV measurements were obtained using a sequence of images obtained with a high-definition camera. The flow was seeded with glass particles (10 μm diameter) and illuminated from the top using LEDs. The recorded images were analyzed using PIVLab software (Thielicke and Stamhuis, 2014). Figure 1.1 shows an illustration of the experimental setup.

1.3 Numerical quasi-two dimensional model

The numerical model considers a change of reference system so that the permanent magnet is fixed while the rectangular container with the liquid moves with a constant velocity along the symmetry axis of the channel. The square magnet whose side length L is much smaller than the distance between lateral walls, is placed beneath the bottom wall of the container with an orientation such that the resulting Lorentz force oppose the oncoming flow. Since the layer thickness is small compared with horizontal dimensions, we use a quasi-two-dimensional (Q2D) model that only considers the normal component of the applied magnetic field. Figure 1.2 shows a sketch of the considered problem.
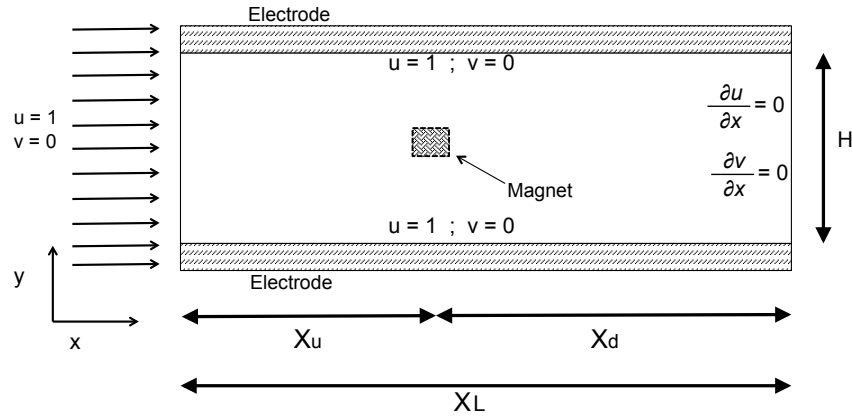

Figure 1.2: Sketch of the problem and boundary conditions.

The model is obtained by averaging of the equations of motion in the transversal z-direction and the effect of boundary layers at the bottom wall is introduced through a linear friction term (Román et al., 2015). Due to the low conductivity of electrolytes, induced effects are negligible so, in dimensionless form, governing equations reduce to

$$\frac{\partial u}{\partial x} + \frac{\partial v}{\partial y} = 0, \tag{1.1}$$

$$\frac{1}{Re}\frac{\partial u}{\partial t} + \left(u\frac{\partial u}{\partial x} + v\frac{\partial u}{\partial y}\right) = -\frac{1}{Re}\frac{\partial P}{\partial x} + \frac{1}{Re}\nabla_{\perp}^2 u + \frac{u}{\tau} - \frac{Ch}{\epsilon\delta}B_z^0, \tag{1.2}$$

$$\frac{1}{Re}\frac{\partial v}{\partial t} + \left(u\frac{\partial v}{\partial x} + v\frac{\partial v}{\partial y}\right) = -\frac{1}{Re}\frac{\partial P}{\partial y} + \frac{1}{Re}\nabla_{\perp}^2 v + \frac{v}{\tau}, \tag{1.3}$$

where velocity components, u and v, are normalized by U, while pressure, P, is normalized by $\rho\nu U/L$. Here, U and L are the velocity and side length of the magnet, respectively. In the fourth term of Eq. (1.2), corresponding to the Lorentz force, the applied current density j and magnetic field B_z^0, are normalized by I/hX_L and B_{max}, respectively, where I, B_{max}, h, and X_L are the applied current intensity, the maximum magnetic field strength, the layer thickness, and the total length of the container, respectively. Dimensionless coordinates x and y are normalized by L, while time, t, is normalized by L^2/ν, while the subindex $\perp$ denotes the projection of the ∇ operator on the x-y plane. The non-uniform magnetic field $B_z^0(x, y, z)$ is modeled by a dipolar field distribution created by square magnetized surfaces uniformly polarized in the normal direction, for which an explicit analytical expression is available (Cuevas et al., 2006a). Finally, $Re = UL/\nu$ is the Reynolds number, which estimates the ratio of inertia to viscous forces, $Ch = IB_{max}L/\rho\nu^2$ is the Chandrasekhar number that represents the ratio of Lorentz to viscous forces (Duran-Matute et al., 2011), and $\epsilon = h/L$ and $\delta = X_L/L$ are the aspect ratios that characterize the geometry of the flow domain. The third term on the right-hand-side of Eqs. (1.2) and (1.3) represents the Rayleigh friction that involves a characteristic dimensionless time scale τ, for the decay of vorticity due to dissipation in the viscous layers which is given by

$$\tau^{-1} = \frac{1}{\epsilon^2 Re} \frac{\gamma(1 - \mathrm{e}^{-\gamma})}{\frac{1}{\gamma}(1 - \mathrm{e}^{-\gamma}) + \frac{\gamma}{2}\mathrm{e}^{-\gamma} - 1}, \tag{1.4}$$

where $\gamma = 0.51$ is an empirical constant that quantifies the decay of the magnetic field through the layer thickness (Román et al., 2015). As boundary conditions (see Fig. 1.2), at the entrance we consider a uniform flow imposed in the x-direction, therefore

$$u = 1, \quad v = 0, \qquad \text{at } x = 0, \quad 0 \leq y \leq H. \tag{1.5}$$

At the outlet, Neumann boundary conditions are used, that is,

$$\frac{\partial u}{\partial x} = \frac{\partial v}{\partial x} = 0, \qquad \text{at } x = X_L, \quad 0 \leq y \leq H. \tag{1.6}$$

Besides, we assume that the side walls move with the entrance constant velocity:

$$u = 1, \quad v = 0, \qquad \text{at } y = 0, H, \quad 0 \leq x \leq X_L. \tag{1.7}$$

Here, H is the separation between lateral boundaries which determines the solid blockage ($\beta = 1/H$) of the confined flow. A finite volume method implemented with a SIMPLEC algorithm is used to solve the governing equations (1.1)-(1.4) with boundary conditions (1.5)-(1.7). A rectangular domain with a length of X_L=40 dimensionless units in the streamwise direction and H=16 units in the cross-stream direction, using an equidistant orthogonal grid of 212×202 nodes, was considered. Upstream distance $X_u = 10$ and downstream distance $X_d = 30$ guarantee that results are nearly independent of the location of the magnet.
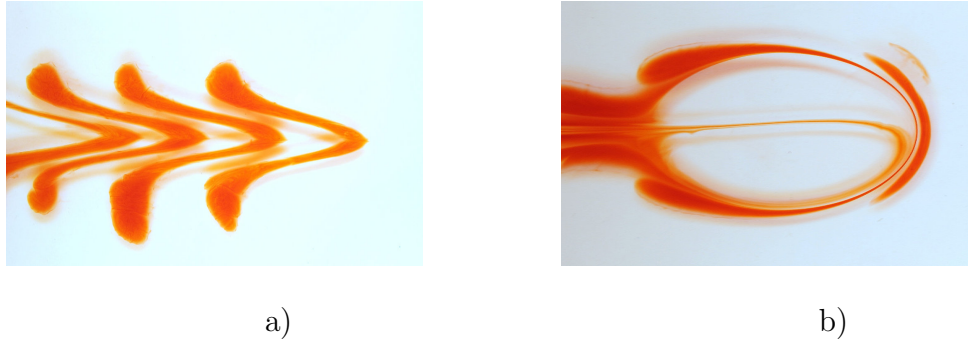
a)	b)

Figure 1.3: Experimental dye visualization of the flow pattern for $Re = 500$. a) Jet-like flow: $Ch = 2.6 \times 10^6$. b) Travelling vortex dipole: $Ch = 5.02 \times 10^6$.

1.4 Experimental and numerical results

In this section we analyze the experimental flow patterns produced by the travelling localized Lorenz force for different values of the magnet velocity and applied current and show the comparison with numerical simulations. Since the velocity of the magnet took values from 0.19 cm/s to 11.1 cm/s, the Reynolds number varied in the range $48 < Re < 2800$. In turn, with the explored range of applied current (0.5 to 5 A), the corresponding range of values taken by Chandrasekhar number was $2.33 \times 10^6 < Ch < 1.63 \times 10^7$. In all cases, the travelling magnet goes from left to right and the aspect ratios are $\epsilon = 0.11$ and $\delta = 39.37$. Figure 1.3 shows the visualization of flow patterns obtained for Re=500 and two different values of Ch. When $Ch = 2.6 \times 10^6$, a jet-like flow was observed (Fig. 1.3a) while the increase of this parameter to $Ch = 5 \times 10^6$, results in the formation of a travelling vortex dipole (Fig. 1.3b). If the Chandrasekhar number is increased up
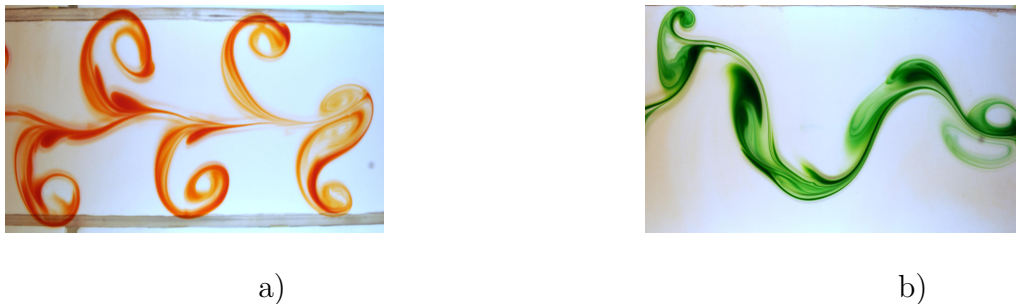

a)	b)

Figure 1.4: Experimental dye visualization of the flow patterns for $Ch = 1.16 \times 10^7$. a) 2P wake: Re=500. b) Bénard-von Kármán wake: Re=800.

to $Ch = 11.6 \times 10^6$, a vortex shedding pattern is observed, displaying a 2P wake where two vortex pairs are shed per oscillation period, as is shown in Fig. 1.4a). This kind of wake has been observed, for instance, in flows produced by a flapping foil in a vertical soap film (Schnipper et al., 2009). In order to explore the transition of the wake as

the Reynolds number is increased, the former value of the Chandrasekhar number was fixed to guarantee that vortex shedding is present. For values of the Reynolds number of 600 and 700 , the vortex pattern still showed two vortex pairs per oscillation period although the wake was deformed. When Re reached 800, the wake transformed into a classical Bénard-von Kármán wake where only two vortices were shed per oscillation period (see Fig 1.4b). Figures 1.5a) and 1.5b) show the velocity fields obtained from PIV measurements for $Re = 500$ (2P wake) and $Re = 800$ (BvK wake), respectively, where a green dot indicates the position of the center of the travelling magnet. As the magnet travels a vortex dipole is formed in front of it, as is observed in both figures although in Fig. 1.5b) the vortex dipole is tilted down. The difference for each Reynolds number lies in the way that vortices are shed. In Fig. 1.5a), the pair of counter-rotating vortices that was shed in half oscillation period is observed below the center of the magnet, in the lower-left part. On the other hand, in Fig. 1.5b), only one elongated vortex shed in half oscillation period is observed behind the center of the magnet.
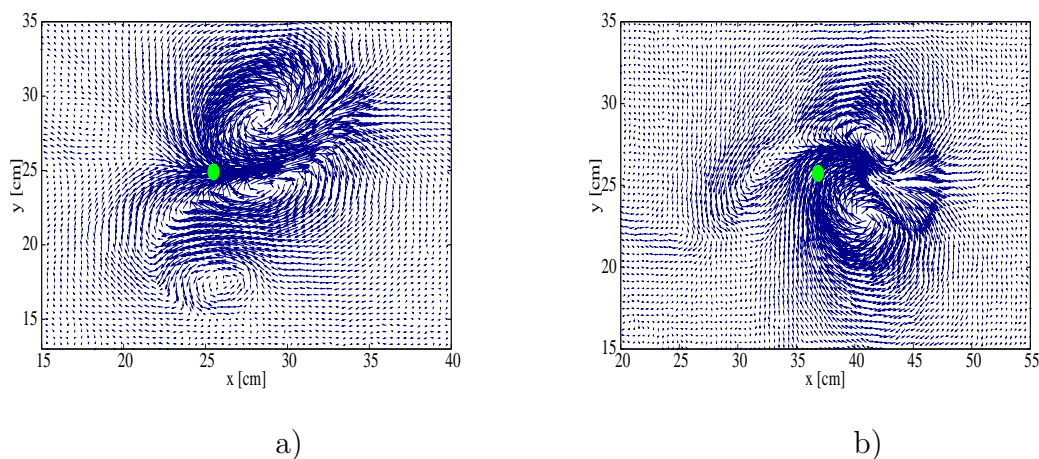

a) b)

Figure 1.5: Experimental velocity fields of the flow patterns for Ch=1.16 × 10^7. a) 2P wake: Re=500. b) Bénard-von Kármán wake: Re=800. The green circle indicates the location of the magnet center.

The structure of the wakes is more clearly understood by analyzing the time evolution of the vorticity. Figures 1.6 and 1.7 show snap shots of the vorticity distribution obtained from PIV measurements for both 2P and BvK wakes, respectively, during one oscillation period. Figure 1.6 shows how positive vorticity (red color) is dragged from the upper lobe towards the lower region forming a vortex dipole that is later shed, while negative vorticity (blue color) is dragged from the lower lobe towards the upper region to form another vortex dipole that is finally shed. In this way, vorticity of different sign is interchanged in one oscillation period. In contrast, in the BvK wake shown in Fig. 1.7, positive and negative vortices are shed alternately from the upper and lower regions without dragging vorticity as in the 2P wake.

In Figs. 1.8a) and 1.8b) the plot of vorticity as a function of time measured with PIV at a fixed point behind the magnet is shown for $Re = 500$ and 800, respectively ($Ch =$
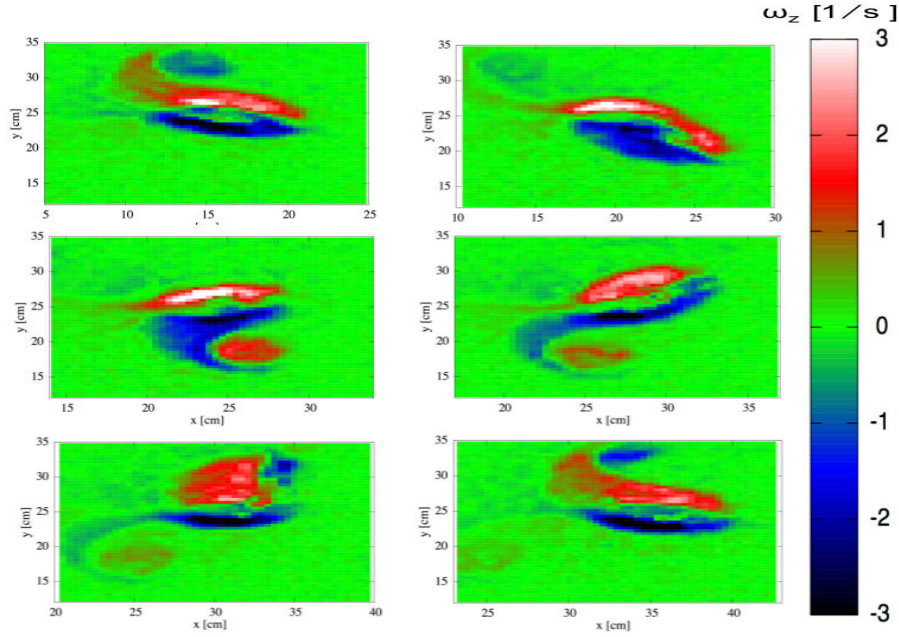
Figure 1.6: Snap shots of vorticity distribution corresponding to the 2P wake obtained from PIV measurements during one oscillation period. $Ch = 1.16 \times 10^7$ and $Re = 500$.

1.16×10^7). In Figure 1.8a), it can be appreciated that for Re=500 two vorticity pulsations appear during one oscillation period. A first pulsation appears in the time interval $20 < t < 25$ and a more intense one shows up in the interval $32 < t < 40$. These two pulsations with positive and negative vorticity peaks manifest the shedding of two vortex pairs per oscillation period that characterizes the 2P wake (Schnipper et al., 2009). In contrast, Fig. 1.8b) shows only one vorticity pulsation during one oscillation period for $Re = 800$ (see the intervals $12 < t < 20$ and $22 < t < 26$) indicating the shedding of two vortices per period, typical of Bénard von Kármán wake (Schnipper et al., 2009).

Figure 1.9 shows the flow transition map, obtained from experimental visualization, built by fixing the Reynolds number and rising the Chandrasekhar number. Although it does not cover the full range of Reynolds number explored, it characterizes the main flow patterns observed. Note that for $Re = 300$ and 400 the travelling vortex dipole found at the lowest Ch value becomes a 2P wake as Ch grows. In turn, for $Re = 500$ and 600, the flow patterns change from a jet-like flow to a travelling vortex dipole as Ch increases; as this parameter grows even further, a vortex shedding with a 2P wake is observed. On the other hand, from $Re = 700$ to 1000, the jet-like flow and the travelling dipole are still found but as Ch is increased further vortex shedding appears in the form of a BvK wake. In fact, for $Re = 700$ the BvK wake transforms into a 2P wake for higher values of Ch. It was also found that the higher Re, the higher the value of Ch required to observe the transition to a wake with vortex shedding. From $Re = 1100$ to 1300 only the jet-like flow and the travelling vortex dipole are observed. It is also illustrative to observe the different flow transitions by fixing Ch and increasing the Reynolds number. In this way,
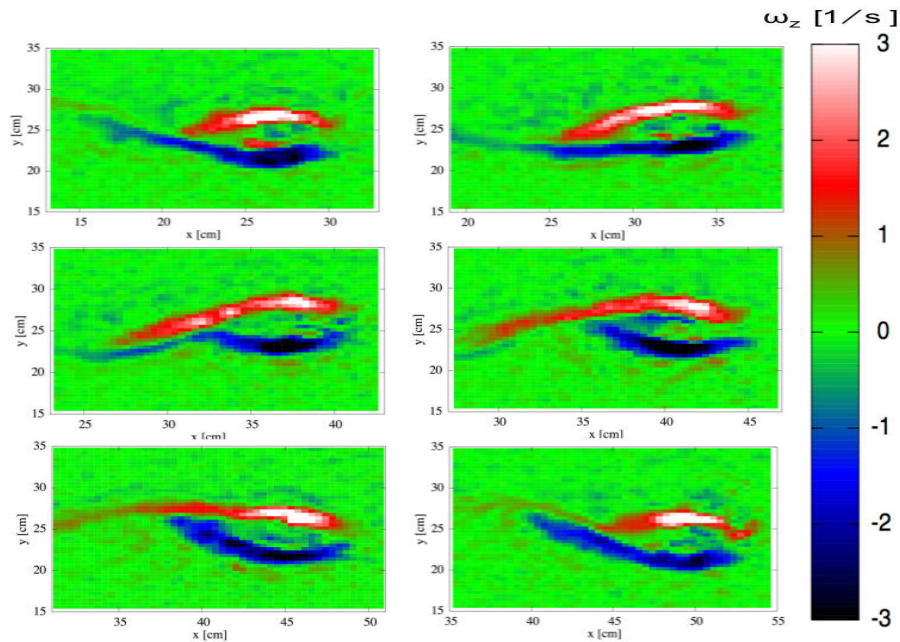
Figure 1.7: Snap shots of vorticity distribution corresponding to the BvK wake obtained from PIV measurements during one oscillation period. $Ch = 1.16 \times 10^7$ and $Re = 800$.

for low values of Ch a travelling vortex dipole becomes a jet-like flow as Re increases. The transitions 2P wake - travelling vortex dipole - jet-like flow and 2P wake - BvK wake - travelling vortex dipole - jet-like flow are also found as Ch takes higher values. This means that for a fixed Ch, the effect of the electromagnetic braking force (*i.e.* the magnetic obstacle) become less important as the flow inertia increases. Results show the clear trend that for a sufficiently high Re, inertia overcomes the braking Lorentz force and vortex patterns disappear, while the flow recovers stability manifested in a jet-like flow. This phenomenon has been recently reported in liquid metal duct flows past a magnetic obstacle Domínguez et al. (2015) and will be presented in chapter 5.

The previous behaviour is clearly reproduced by the numerical model. By following the procedure of Domínguez et al. (2015), we define the amplitude $\mathcal{A}$ of the transversal velocity oscillation v with respect to its average value $\langle v \rangle$ over the interval I at a given point, that is, $\mathcal{A} = v - \langle v \rangle$. In order to quantify the main contribution to the kinetic energy of the flow, it is introduced the parameter $\mathcal{L}^2$, defined as

$$\mathcal{L}^2 = \frac{1}{I} \int_0^I \mathcal{A}^2 dt, \tag{1.8}$$

where $\mathcal{L}^2$ is a function of the Chandrasekhar and Reynolds numbers and indicates the average of the square of the amplitude $\mathcal{A}$ in the interval I. Figure 1.10 shows the parameter $\mathcal{L}^2$ as a function of the Reynolds number for $Ch = 1.16 \times 10^7$, obtained from numerical results at the point $x = 16$, $y = 8$, located at the mid line of the channel 6 unities downstream the magnet. The interval I corresponds to 40 oscillation periods. From

$Re = 300$ to $Re = 600$, the parameter $\mathcal{L}^2$ increases as the Reynolds number increases. As observed from the experimental map (Fig. 1.9), this zone correspond to the 2P wake. Note that the transition from 2P wake to BvK wake found in Fig. 1.9 from $Re = 600$ to $Re = 700$ is reproduced in the numerical simulation shown in Fig. 1.10 as a change in the slope of the curve for the same interval of Reynolds numbers. The second change in the slope direction appears for $Re = 900$, corresponding to the transition from BvK wake to the travelling vortex dipole, where $\mathcal{L}^2$ has its maximum value; beyond this critical value, as Re increases the parameter $\mathcal{L}^2$ starts decreasing. Finally, the transition from the travelling vortex dipole to the jet-like flow found experimentally from $Re = 1000$ to $Re = 1100$ (see Fig. 1.9), is also found numerically as a change in the slope in Fig. 1.10 but with a slight shift (from $Re = 1100$ to $Re = 1200$).

More detailed numerical results are displayed in Fig. 1.11 where vorticity distributions of 2P and BvK wakes for the parameter values used for results presented in Fig. 1.8 are shown. Aside, the vorticity as a function of time at a given point is shown for each case. Numerical results show qualitative agreement with the main features observed in the experiment. In fact, the shedding of a vortex dipole which is a feature of the 2P wake, as well as the alternated vortex shedding, characteristic of the BvK wake, are clearly observed.
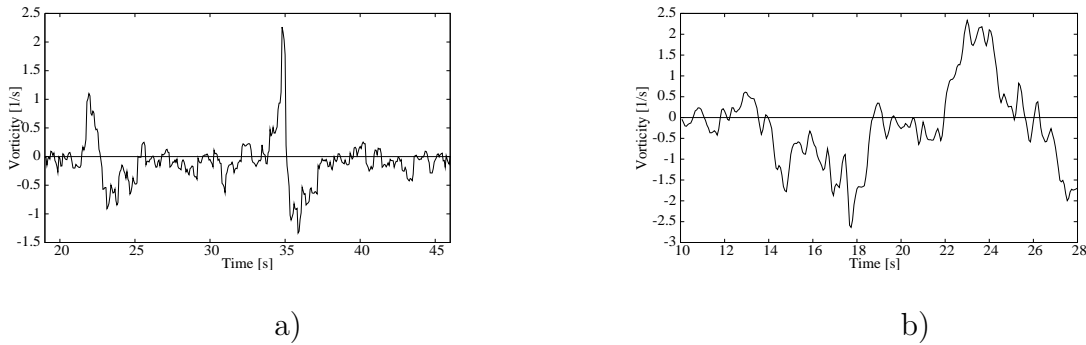

a)   b)

Figure 1.8: Vorticity as a function of time for $Ch = 1.16 \times 10^7$ measured with the PIV method. a) At a point on the symmetry axis 8 cm behind the magnet for $Re = 500$. b) At a point 2 cm above the symmetry axis and 8 cm behind the magnet $Re=800$.

1.5   Conclusions

Wake patterns created by a travelling localized Lorentz force in a shallow electrolyte layer have been studied experimentally and numerically. The variation of the Reynolds and Chandrasekhar numbers allowed to observe four characteristic patterns, namely, jet-like flow, travelling vortex dipole, 2P wake and BvK wake. The time evolution of the vorticity distribution showed the main features of the wakes such as the shedding of two vortex pairs per oscillation period in the case of 2P and the shedding of two alternate vortices per oscillation period in the case of BvK. A map of qualitative flow behavior as function
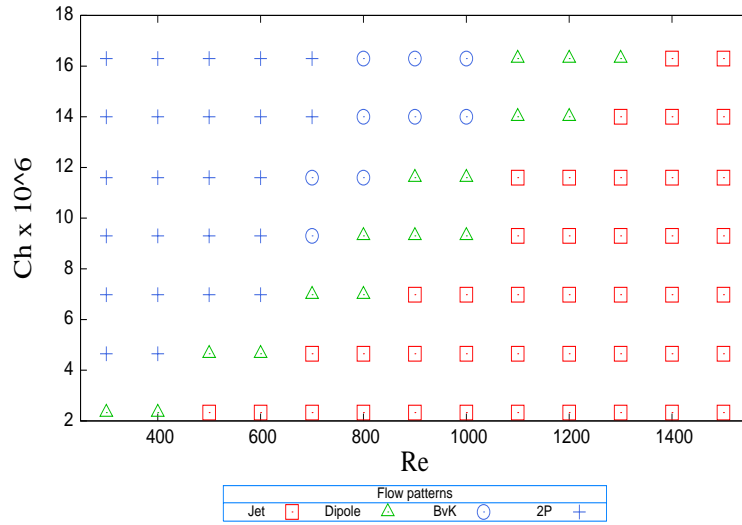
Figure 1.9: Experimental flow transition map for different values of the governing flow parameters, namely, Chandrasekhar and Reynolds numbers.

of the governing parameters shows different transitions that occur among the observed flow patterns. It is interesting to note that for a fixed Chandrasekhar number, the jet-like flow is always found for a high enough Reynolds number indicating that inertia overcomes the electromagnetic braking force. This behavior is also found from the numerical model through the calculation of the parameter $\mathcal{L}^2$ related with the main contribution to the kinetic energy of the flow which also detects the flow transitions observed experimentally. Although numerical results reproduce the characteristic flow behavior, some limitations of the model were found at Reynolds numbers higher than 1100.
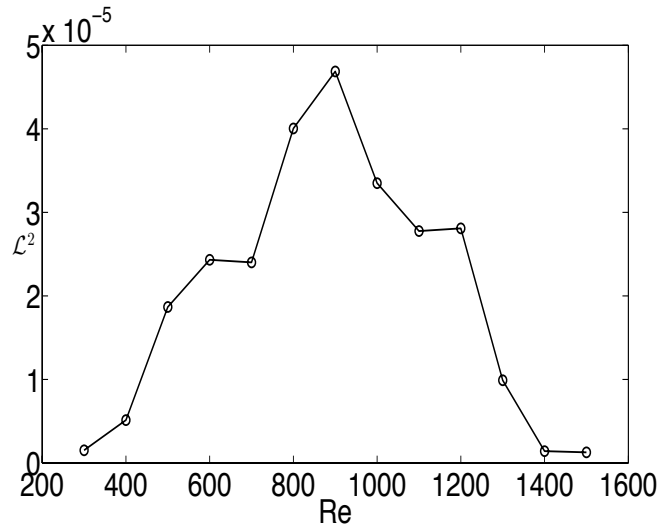
Figure 1.10: The parameter $\mathcal{L}^2$ as a function of the Reynolds number for $Ch = 1.16 \times 10^7$ obtained from numerical results.

Figure 1.11: Numerical vorticity distribution and vorticity as a function of time at a point for $Ch=1.16 \times 10^7$. For $Re = 500$, at a point on the symmetry axis 8 cm behind the magnet and for $Re=800$ at a point 2 cm above the symmetry axis and 8 cm behind the magnet. a) and b) 2P wake: $Re=500$. c) and d) BvK wake: $Re=800$.

Numerical study of wake patterns behind a pair of magnetic obstacles in an electrolyte layer

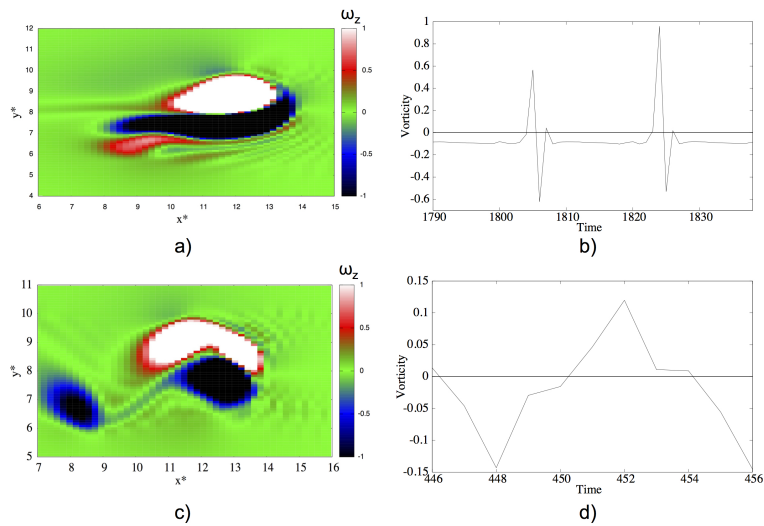In this Chapter[1], we present the quasi-two-dimensional numerical simulation of the flow in a thin layer of electrolyte past a pair of localized Lorentz forces, named *magnetic obstacles*, placed side by side. Opposing Lorentz forces are produced by the interaction of the magnetic field created by a pair of small permanent magnets and a D.C. current applied transversally to the main flow. By varying the separation between the magnets and the intensity of the applied current different flow regimes are analyzed. The attention is focused in the interference of the wakes created by the magnetic obstacles.

2.1 Introduction

The flow past solid obstacles is certainly one of the most widely studied problems in fluid dynamics and constitutes in itself a classic subject of research (Zdravkovich, 1997). Its importance stems from countless applications where determining the behavior of flows past bluff bodies is of practical interest. From the point of view of dynamical system, the understanding of the spatiotemporal behavior of the wakes formed in flows past solid obstacles presents interesting challenges. When more than one obstacle is present, to investigate the interference of wakes becomes a relevant issue (Le Gal et al., 1996). In fact, the behavior of coupled wakes created by a pair of cylinders placed side by side in a uniform flow has been studied experimentally and theoretically by several authors and different flow regimes have been identified according to the separation between the cylinders (Zdravkovich, 1985; Le Gal et al., 1990; Peschard and Le Gal, 1996; Sumner et al., 1999). But wakes are not only produced by solid obstacles. It has been shown that localized magnetic forces in flows of electrically conducting fluids act as obstacles for the flow. When the conducting fluid is a liquid metal, the relative motion of the fluid and a localized magnetic field induces electric currents that interact with the same field to produce a Lorentz force that brakes the liquid (Cuevas et al., 2006*a*; Votyakov et al., 2007).

---

[1]This Chapter is mainly based on the paper: Román, J.; Beltrán, A.; Cuevas, S. "Numerical Simulation of the Flow Past a Pair of Magnetic Obstacles". Selected Topics of Computational and Experimental Fluid Mechanics. Springer International Publishing, 2015. p. 415-425.

In the case of an electrolyte, due to the low conductivity of the fluid, induced currents are negligible but an opposing Lorentz force can still be created if an electric current is externally applied (Honji, 1991; Honji and Haraguchi, 1995; Afanasyev and Korabel, 2006*b*). In both cases, experimental and theoretical studies have shown the appearance of different flow regimes such as steady vortices, vortex shedding, and even turbulent wakes (Honji and Haraguchi, 1995; Afanasyev and Korabel, 2006*b*; Votyakov et al., 2008; Kenjeres et al., 2011). In fact, the term *magnetic obstacle* was coined (Cuevas et al., 2006*a*) to emphasize that localized Lorentz forces produce flow behaviors that in some aspects resemble flows past solid obstacles, although very important differences exist.

So far, investigations of flows past magnetic obstacles have mainly addressed the problem of a single obstacle in liquid metal flows (see, for instance, Votyakov et al. (2008); Kenjeres et al. (2011); Tympel et al. (2013)). Recently, the flow in an array of three magnetic obstacles has been simulated numerically (Kenjeres, 2012), a situation that may have relevance for heat transfer applications (Zhang and Huang, 2013). Flows of electrolytes past magnetic obstacles have been less explored. Honji (1991) and Honji and Haraguchi (1995) performed experiments in a shallow layer of salt water contained in a long tank, where a D.C. current was applied transversally to the tank's long axis while a permanent magnet located externally was dragged at a constant velocity along the center line of the water tank. Similar but more extensive experiments were performed by Afanasyev and Korabel (2006*b*). These authors considered flows produced by a single magnet as well as by two magnets with opposite orientations, aligned with the direction of motion and separated by a short distance. However, to the best of our knowledge, the electrolytic flow created by a pair of magnetic obstacles side by side has not been previously considered. This problem is interesting since the analogous flow with solid obstacles has been investigated extensively so that flow regimes are well characterized (Zdravkovich, 1985; Peschard and Le Gal, 1996; Sumner et al., 1999). In the present study, we explore numerically the flow past a pair of magnetic obstacles side by side and compare the flow regimes with those corresponding to the flow past solid cylinders.

2.2   Formulation of the problem

We consider the flow of a shallow layer of an electrolyte in a rectangular container affected by localized Lorentz forces, *i.e.* magnetic obstacles. The forces are produced by the interaction of magnetic fields generated by two permanent magnets and a D.C. electrical current applied transversally to the main flow through electrodes located in the lateral walls and connected to a power source. Square magnets whose side length L is much smaller than the distance between lateral walls, are placed beneath the bottom wall of the container with an orientation such that resulting Lorentz forces oppose the oncoming flow and generate vorticity.
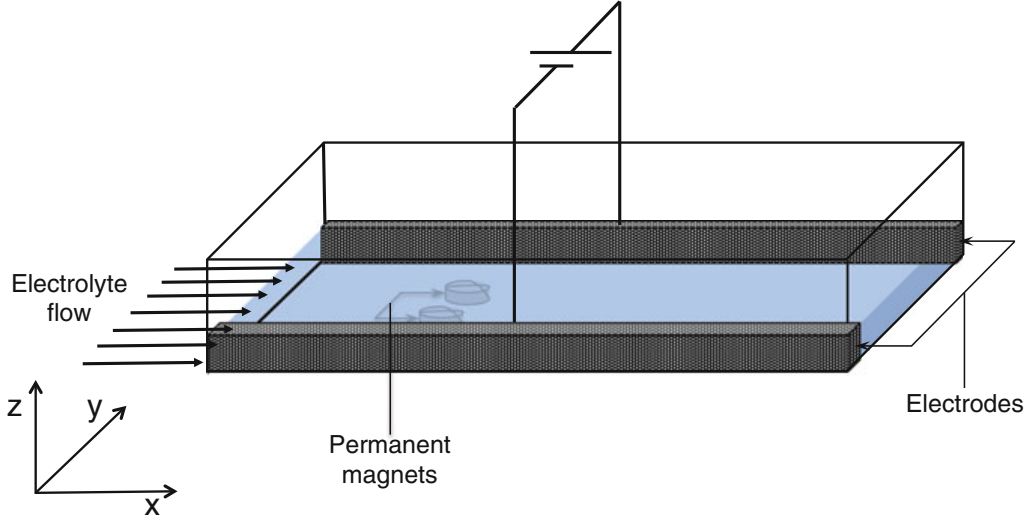
Figure 2.1: Sketch of the electrolytic flow past a pair of magnetic obstacles side by side.

Figure 2.1 shows a sketch of the problem under consideration. Since the thickness of the fluid layer is assumed to be small compared with horizontal dimensions, we use a quasi-two-dimensional (Q2D) numerical model that only considers the component of the applied magnetic field normal to the plane of motion. This component can be expressed as

$$B_z^0(x, y, z) = B(x, y)g(z), \tag{2.1}$$

where $B(x, y)$ reproduces the variation of the magnetic field in the x - y plane and is modeled by a dipolar field distribution created by a square magnetized surface uniformly polarized in the normal direction, for which an explicit analytical expression is available (McCaig, 1977; Cuevas et al., 2006a). In fact, the shape of the magnets is irrelevant provided the plane of flow is separated from the surface of the magnet, so that border effects are smoothed out (Figueroa et al., 2009). In turn, $g(z) = exp(-\gamma z)$ models the decay of the magnetic field in the normal direction z (normalized by the layer thickness h), where $\gamma = 0.51$ is an empirical constant obtained from fitting the decay of the magnetic field in the vertical direction (Beltrán, 2010) with experimental data from a permanent magnet (Honji, 1991). In addition, the Q2D model assumes that the momentum transfer through the thin electrolytic layer is mainly diffusive so that the velocity field can be expressed as

$$\mathbf{u}(x, y, z) = [\bar{u}(x, y, z)f(x, y, z), \bar{v}(x, y, z)f(x, y, z), 0], \tag{2.2}$$

where $\bar{u}$ and $\bar{v}$ are the mean velocity components in the x-y plane, while $f(x, y, z)$ reproduces the velocity profile in the layer thickness (Beltrán, 2010). Since the electrical

conductivity of the electrolyte is low compared with that of liquid metals, and the magnetic field intensity of permanent magnets is weak, induced currents in the fluid are negligible. Therefore, it becomes unnecessary to solve the induction equation to determine the induced magnetic field. Only the applied current is relevant for calculating the Lorentz forces (Figueroa et al., 2009).

Substituting Eqs.(2.1) and (2.2) in the three-dimensional equations of motion and averaging along the height of the fluid layer, we obtain the Q2D equations. A detailed description of the averaging procedure can be found in Beltrán (2010) and Figueroa et al. (2009). In dimensionless terms, the equations of motion in the Q2D approximation take the form

$$\frac{\partial u}{\partial x} + \frac{\partial v}{\partial y} = 0, \tag{2.3}$$

$$\frac{\partial u}{\partial t} + \left(u \frac{\partial u}{\partial x} + v \frac{\partial u}{\partial y} \right) = -\frac{\partial P}{\partial x} + \frac{1}{Re} \nabla_\perp^2 u + \frac{u}{\tau} - Q B_z^0, \tag{2.4}$$

$$\frac{\partial v}{\partial t} + \left(u \frac{\partial v}{\partial x} + v \frac{\partial v}{\partial y} \right) = -\frac{\partial P}{\partial y} + \frac{1}{Re} \nabla_\perp^2 v + \frac{v}{\tau}, \tag{2.5}$$

where the overline in the velocity components was dropped and subindex $\perp$ denotes the projection of the ∇ operator on the x-y plane. The velocity components, u and v, the pressure, P, the applied current density, j, and the applied magnetic field, B_z^0, are normalized by U, ρU^2, j_0 and B_{max}, respectively. Here, U is the uniform entrance velocity, ρ is the mass density, B_{max} is the maximum intensity of the magnetic field, and j_0 is the magnitude of the applied current density. Dimensionless coordinates x and y are normalized by L, while time, t, is normalized by L/U. Dimensionless parameters Re and Q stand for the Reynolds number $Re = UL/\nu$, where ν the kinematic viscosity, and the Lorentz force parameter $Q = J_0 B_{max} L/\rho U^2$ which is the ratio of a magnetic pressure drop caused by the applied Lorentz force and the free-stream dynamic pressure. Essentially, Q characterizes the strength of the Lorentz forces. The third term on the right-hand-side of Eqs. (2.4) and (2.5) represents the Rayleigh friction. It involves a characteristic dimensionless timescale, τ, for the decay of vorticity due to dissipation in the viscous layers and is given by Beltrán (2010).

$$\tau^{-1} = \frac{\gamma(1 - e^{-\gamma})}{\frac{1}{\gamma}(1 - e^{-\gamma}) + \frac{\gamma}{2} e^{-\gamma} - 1}, \tag{2.6}$$

The considered boundary conditions are the following. At the entrance, a uniform flow is imposed in the x-direction, therefore

$$u = 1, \quad v = 0, \qquad \text{at } x = 0, \quad 0 \leq y \leq H. \tag{2.7}$$

At the outlet, Neumann boundary conditions are used, that is,

$$\frac{\partial u}{\partial x} = \frac{\partial v}{\partial x} = 0, \qquad \text{at } x = X_L, \quad 0 \leq y \leq H. \tag{2.8}$$

At the side walls, we use non-slip conditions:

$$u = 0, \quad v = 0, \qquad \text{at } y = 0, H, \quad 0 \leq x \leq X_L. \tag{2.9}$$

Here, H is the separation between lateral boundaries which determines the solid blockage of the confined flow, characterized by the blockage parameter $\beta = 1/H$. In turn, X_L is the total length of the channel. The magnetic obstacles are located at a distances X_u from the entrance and X_d from the outlet. All the lengths are measured in dimensionless units. The centers of the magnets are separated by a dimensionless distance $D = d/L$, where d is the dimensional separation. Figure 2.2 shows a sketch of the flow conditions considered for the numerical solution.
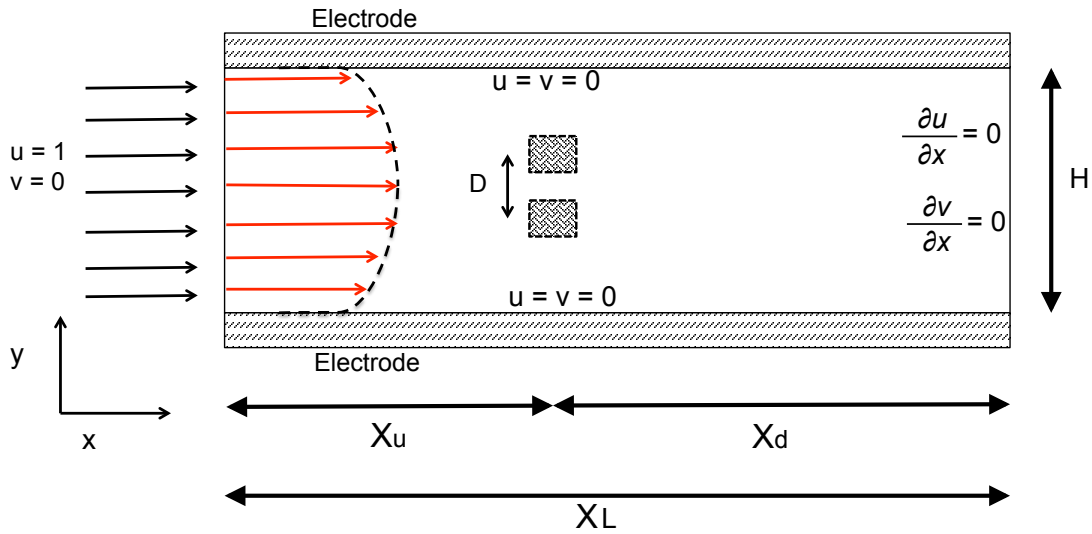

Figure 2.2: Sketch of the geometry and boundary conditions considered for the analyzed flow.

A finite volume method implemented with a SIMPLEC algorithm is used to solve the governing equations (2.3)-(2.6) with boundary conditions (3.10)-(3.12). The diffusive and convective terms are discretized using a central difference scheme. Accurate temporal resolution is provided by choosing a small enough time step and employing a second order scheme for the time integration. The numerical solution was obtained in a rectangular domain with a length of $X_L = 35$ dimensionless units in the streamwise direction and $H = 7$ units in the cross-stream direction using an equidistant orthogonal grid of 212×202 nodes. It was determined that upstream distance $X_u = 10$ and downstream distance $X_d = 25$ guarantee results that are nearly independent of the location of the obstacles.

2.3 Numerical results

In a similar way as when the obstacles are solid cylinders, flows past a pair of magnetic obstacles side by side present different regimes according to the flow conditions. While

hydrodynamic regimes are governed only by the Reynolds number and the dimensionless separation distance D (provided three-dimensional effects are neglected), in the present case flow regimes are controlled by Q, in addition to Re and D. The variation of these parameters leads to steady or time-dependent regimes, as occurs in flows with a single magnetic obstacle (Honji and Haraguchi, 1995; Afanasyev and Korabel, 2006b). We present numerical results for a pair of magnetic obstacles side by side with a fixed Reynolds number, $Re = 1000$, and investigate the variation of Q and D on the flow dynamics. We consider flow conditions where vortex shedding is present and explore the effect of separation distance D in the coupling of the wakes behind the obstacles. The parameter Q is varied in the range $1.5 \leq Q \leq 10$, and for a given D, the value of Q corresponds to the minimum value where vortex shedding appears. In turn, four different values of D are explored, namely, 1, 1.5, 2, and 3, which are of interest since results for the hydrodynamic flow past a pair of solid obstacles are available in the literature for these cases (Peschard and Le Gal, 1996; Zdravkovich, 1985). In hydrodynamic flows, it has been reported that for large distance between the cylinders the pair of wakes presents a weak coupling where in phase and out of phase vortex shedding can appear. In turn, for shorter distances a strong coupling arises and only in phase shedding is observed which produces a unique Bénard-von Kármán street (Peschard and Le Gal, 1996; Zdravkovich, 1985). At intermediate range of coupling, a bistable regime can emerge which is characterized by a biased flow that gives two possible values for the vortex shedding frequency. In this case, the biased flow through the gap divides asymmetric states with narrow and wide wakes which can intermittently interchange between the two cylinders (Zdravkovich, 1985), apparently driven by a random process (Peschard and Le Gal, 1996). We now show that similar regimes are observed in the wakes created by a pair of magnetic obstacles side by side.

Figure 2.3 shows the Lagrangian tracking of flows obtained numerically for different values of D, with the corresponding minimum value of Q where vortex shedding appears. For the smallest separation distance, $D = 1$ (see Fig. 2.3a)), the magnets are in contact and act as a larger magnetic obstacle that gives rise to a single wake similar to the Bénard-von Kármán street. If the gap between the obstacles is increased to $D = 1.5$, we find a bistable regime where the flow pattern is rather complex, as is observed in Fig. 2.3b). A further increase to $D = 2$ (see Fig. 2.3c)) leads to a more structured flow pattern with two interlaced wakes in phase. For the larger gap explored, namely $D = 3$, the separation between the wakes is neatly defined and the in phase behavior still persists, as observed in Fig. 2.3d).
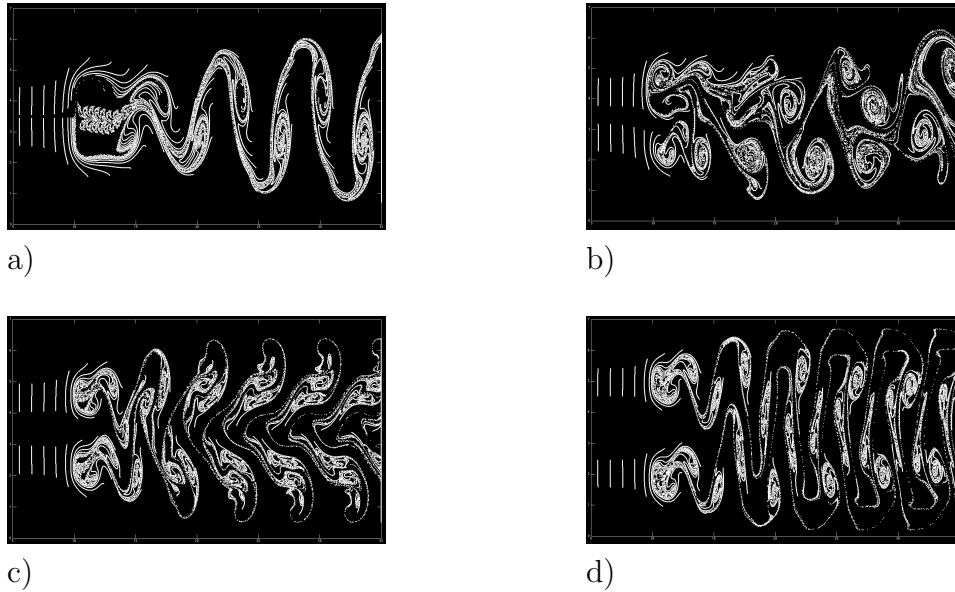
Figure 2.3: Lagrangian tracking of the numerically calculated flow past a pair of magnetic obstacles side by side at different separation distances. $Re = 1000$. a) D =1, $Q = 2.7$. b) D= 1.5, $Q = 2.9$. c) D= 2, $Q = 2.4$. d) D= 3, $Q = 2.3$.

To improve the understanding of the flow behavior and the coupling of the wakes behind the magnetic obstacles, the velocity component in the x-direction is shown in Fig.2.4 as a function of time at two distinct points located on the central line of each obstacle, five dimensionless units downstream. For $D = 1$ (Fig. 2.4a)), corresponding to the single wake of a large magnetic obstacle, the velocity signals oscillate in antiphase. This is consistent with the fact that a large oscillating vortex structure is formed behind the obstacle so that in the symmetrically located points where the signals are registered, the velocity in the x-direction takes opposite values. For $D = 1.5$ that corresponds to the bistable flow, velocity oscillations do not present a defined structure. This seems to be a characteristic feature of this regime as it has been reported in the literature for the case of circular cylinders (Zdravkovich, 1985; Peschard and Le Gal, 1996). Figure 2.4c) clearly shows in phase oscillations of the velocity signals when $D = 2$ where even the amplitude of the oscillations coincides. Finally, when $D = 3$ (Fig. 2.4d)), although velocity oscillations are in phase, amplitudes do not coincide which indicate a weaker coupling of the wakes.
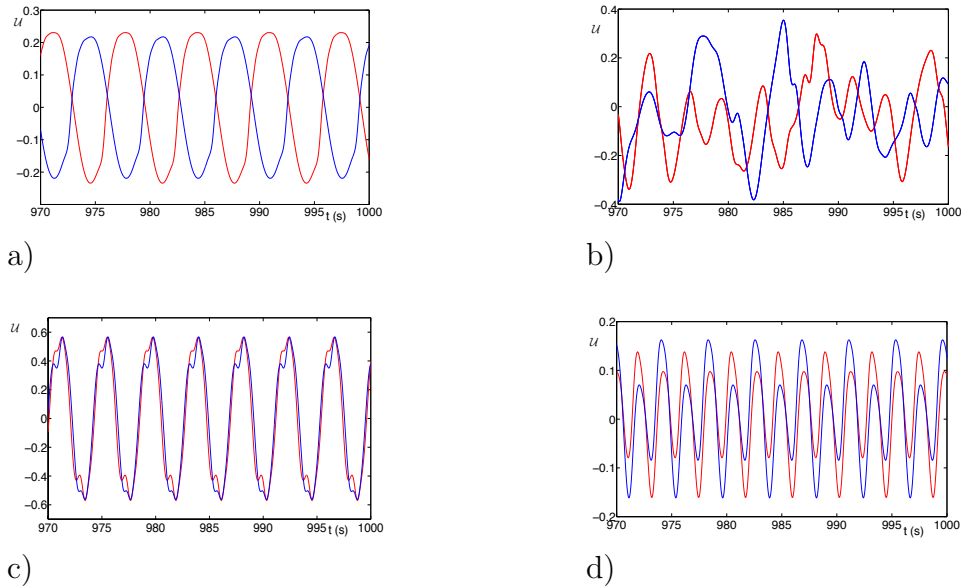
Figure 2.4: Velocity component in the x-direction as a function of time at two different points. Blue (red) line corresponds to the point located at the central line of the upper (lower) obstacle five dimensionless units downstream.. $Re = 1000$. a) $D = 1$, $Q = 2.7$. b) $D = 1.5$, $Q = 2.9$. c) $D = 2$, $Q = 2.4$. d) $D = 3$, $Q = 2.3$.

Important information can also be obtained from the Fourier analysis of the temporal behavior of the velocity signals, particularly for determining the dominant dimensionless frequency of the flow, that is, the Strouhal number. It is precisely at this frequency at which the greatest amount of energy in the flow is transported. Figure 2.5 shows the power spectrum obtained through the fast Fourier transform of the corresponding velocity signals presented in Fig. 2.4 for different values of D. Only the spectrum at one point is shown since it coincides with the one at the other point. In Fig. 2.5a) ($D = 1$), a clear dominant characteristic frequency of 0.152 and its corresponding harmonics are shown. This frequency is close to the ones obtained experimentally by Honji and Haraguchi (1995) for the flow past a single magnetic obstacle. Further, it almost coincides with the value of 0.150 corresponding to the flow past a solid cylinder (Zdravkovich, 1997). For the bistable flow at $D = 1.5$ (Fig. 2.5b)), it does not exist a clear dominant frequency since this local analysis does not capture the global behavior of the biased flow that may present two distinct characteristic frequencies for the vortex shedding. Finally, Figs. 2.5c) and 2.5d) display very similar Strouhal numbers of 0.235 and 0.237 for $D = 2$ and $D = 3$, respectively. It could be expected that for a large enough separation distance, the dominant frequency of each wake should be close to that of a single magnetic obstacle (≈ 0.152). The difference with the latter case for $D = 2$ and $D = 3$ manifest that the coupling of the wakes is still present at these separation distances. In fact, for the flow past a pair of solid cylinders side by side, the uncoupling of the wakes is observed at $D \approx 5.5$ (Le Gal et al., 1990).
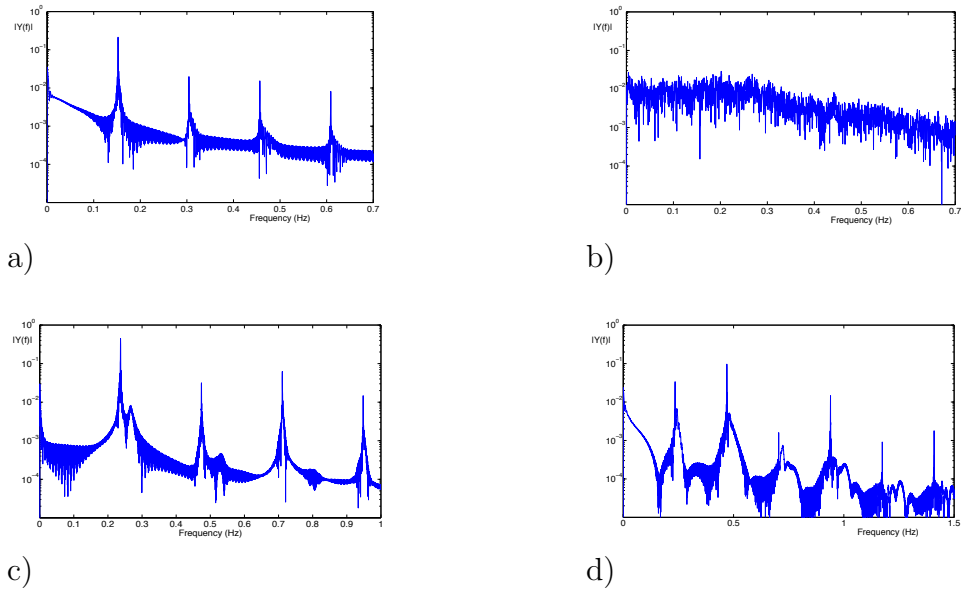
Figure 2.5: Power spectrum calculated by the Fast Fourier Transform of the velocity signals presented in Fig. 2.4. $Re = 1000$. a) $D = 1$, $Q = 2.7$. b) $D = 1.5$, $Q = 2.9$. c) $D = 2$, $Q = 2.4$. d) $D = 3$, $Q = 2.3$.

A characteristic feature of the bistable regime is the tendency of the flow in the gap between the obstacles to tilt towards one obstacle at a given time and towards the other obstacle at a later time. This deflection breaks the symmetry of the flow pattern (Le Gal et al., 1990). Figure 2.6 illustrates this phenomenon through the instantaneous velocity fields at two different times for the bistable regime observed when $D = 1.5$.
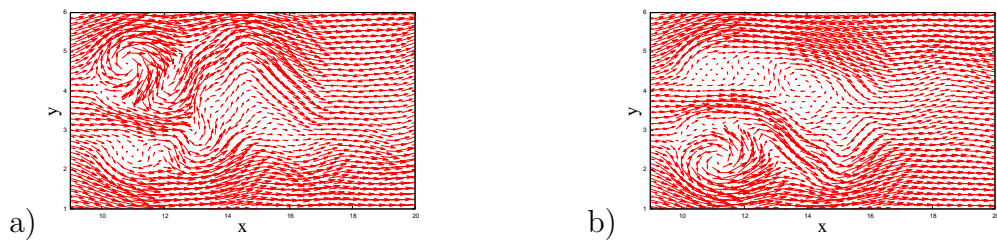

Figure 2.6: Instantaneous velocity fields for the bistable regime. $Re = 1000$, $Q = 2.9$ and $D = 1.5$. a) $t = 1975$, b) $t = 1992$.

Although in previous results only time-dependent flows were considered, at lower values of Q steady flow patterns displaying a vortex pair are found (Román, 2013). With the aim of describing the studied flow in a more complete way, Fig. 2.7 presents a map that shows the regions of steady and time-dependent behavior in terms of the analyzed values of Q and D, for $Re = 1000$. The transition zone between steady and unsteady flows is presented with a gray strip since it is not possible to determine an exact value for this

transition. This map is built based on the time behavior of the velocity signals. It is observed that for a fixed D, vortex shedding disappears as Q decreases.
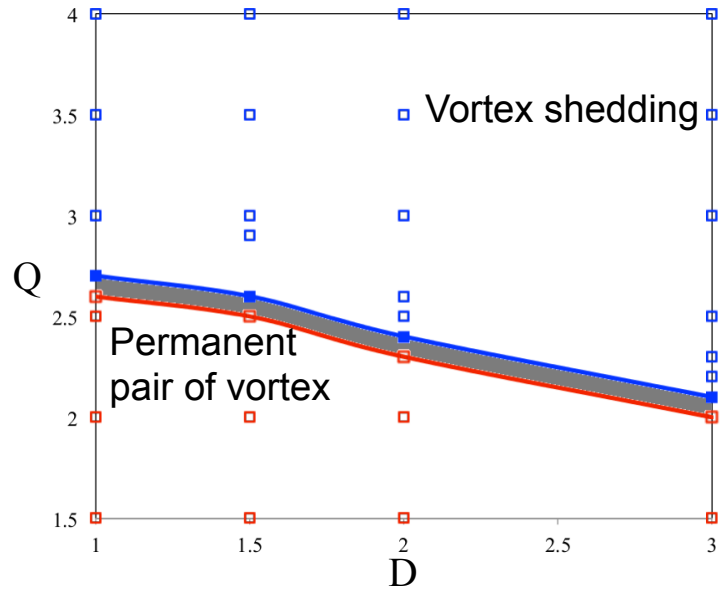

Figure 2.7: Flow transition map of the flow past a pair of magnetic obstacles side by side. The gray strip displays the transition zone between steady and time-dependent flow. $Re = 1000$.

2.4 Concluding remarks

In this Chapter, we have investigated numerically using a Q2D model the flow past a pair of magnetic obstacles side by side at a fixed Reynolds number, $Re = 1000$. We analyzed the coupling of the wakes behind the magnetic obstacles under vortex shedding conditions for different values of the dimensionless separation distance, namely, $D = 1$, 1.5, 2, and 3. From the numerical velocity field, Lagrangian trajectories were obtained which allow to visualize different flow structures. A strong coupling was found for $D = 1$ where the pair of obstacles act as a large magnetic obstacle that produces a single wake whose dominant frequency is close to the one found experimentally (Honji and Haraguchi, 1995) and almost coincide with that of the flow past a solid cylinder. A more complex pattern was found for $D = 1.5$ where an intermediate coupling leads to a bistable regime, characterized by a biased flow with asymmetric flow structures. Finally, a weaker coupling of the wakes was found for $D = 2$ and $D = 3$, where well defined in-phase wakes are observed. In general terms, it can be stated that the flow past a pair of magnetic obstacles side by side present similar regimes as those observed in the wakes created by a pair of solid cylinders.

Flow past a magnetic obstacle in a narrow channel

In this Chapter[1], a theoretical-experimental study of the flow past a magnetic obstacle in a narrow channel is presented. The experimental setup and methodology are very similar to those presented in Chapter 1 but in this case the attention is focused on the effect of the lateral walls on the flow patterns. Numerical simulations using a quasi-two-dimensional model agree qualitatively with experimental visualizations. Further, flow transition maps built from experimental and numerical results are presented.

3.1 Vortex streets in a narrow channel

The vortex wakes generated in the flows past solid obstacles have been widely studied. The main configuration is the unbounded fluid flow past a solid cylinder which remains fixed. Another case of study is the interaction of two or more wakes (Zdravkovich, 1985, 1997; Le Gal et al., 1996) promoted by two or more solid obstacles. With the aim of understanding the mechanism of vortex wake generation, Godoy-Diana et al. (2008) presented a study of flow pattern transition using a moving airfoil as the obstacle in a wind tunnel. In the cited work, the authors reported three flow patterns: the Bénard-von Kármán street (BvK), aligned vortices and reverse Bénard-von Kármán street (rBvK). The latter is a wake vortex street with the sign of vorticity of each vortex inverted with respect to the typical Bénard-von Kármán. But flow transitions can also occur when the wake interacts with the confining walls. In fact, the interaction of vortex streets with the side walls has been widely studied. This case is of particular importance because of their potential application in heat transfer enhancement. Davis et al. (1984) presented a numerical and experimental study of the oscillation of the wake and the drag coefficient for two different values of the blockage parameter β, that is, the relationship between the obstacle's length in crosswise direction and the distance between the channel walls. They found that the drag coefficient and the oscillation frequency of the wake increase as the blockage parameter increases. Camarri and Giannetti (2007) studied the inversion of the BvK street behind a square solid obstacle for a blockage parameter within the range $\frac{1}{10} \leq \beta \leq \frac{1}{6}$. They showed that the inversion of the BvK street appears at a fixed distance behind of the solid obstacle

---

[1]This Chapter is mainly based on the paper: Roman, J., Uriostegui, K, Guerrero, W., Figueroa, A., Vázquez, F., Cuevas, S., 2017, "Vortex streets in a narrow channel". In preparation.

which depends on the Reynolds number Re and the blockage parameter. Singha and Sinhamahapatra (2010) investigated the behavior of the vortex street in a confined region at within the range $50 \leq Re \leq 250$. They found that for a small blockage a larger Re is required to get vortex shedding, which indicates that small values of the blockage parameter increase the flow stability. In turn, Wang and Alben (2015) studied numerically the effect of the side walls on both the BvK street and the rBvK street regardless of how the flow patterns are generated. In order to do so, they imposed as an input condition the flow patterns through an analytical solution. When the input flow was a rBvK street, the flow pattern did not change along the channel, unlike what happened with the BvK, where vortices moved away from the wall so that they crossed the symmetry axis of the solid obstacle. In fact, a vortex with positive vorticity that initially was below the symmetry axis moved above that axis, while a vortex with negative vorticity placed above the axis moved below it.

As we have shown in previous chapters, localized electromagnetic forces, named magnetic obstacles, are an alternative to the use of solid obstacles to generate vortices. (Cuevas et al., 2006a; Votyakov et al., 2007). The braking force generated by the interaction of electric currents and applied magnetic fields is able to create vorticity and lead to the generation of wake patterns. For instance, different flow patterns such as steady vortices and vortex shedding appear in many experimental and theoretical studies (Cuevas et al., 2006a,b; Votyakov et al., 2007; Beltrán, 2010; Kenjeres et al., 2011; Votyakov et al., 2008; Tympel et al., 2013; Kenjeres, 2012; Zhang and Huang, 2013). The majority of the studies involve liquid metal flows such as the one by Votyakov et al. (2008) who performed experiments and numerical simulation of the flow of liquid metal past a magnetic obstacle in a duct. These authors studied the effect of what they defined as the constrainment factor κ, which coincides with the definitions of the blockage parameter, that is, is, the ratio between the characteristic length of the external magnet and the separation between the wall ducts in the spanwise direction. They reported different flow patterns depending on the value of the constrainment factor, namely, a vortex dipole for $\kappa = 0.02$, a six-vortex pattern for $\kappa = 0.4$, and no vortex pattern for $\kappa = 1.0$. On the other hand, Zhang and Huang (2013) performed a numerical simulation of the flow of liquid metal past an array of three magnetic obstacles. They studied the fluid dynamics and the heat transfer considering the blockage parameter and reported that for $\beta = 0.2$ the effect of the side walls is negligible. For values between $0.2 < \beta < 0.4$ the flow pattern is highly influenced by the side wall, while for $\beta = 0.4$, the jet flow between the side wall and the magnetic obstacles governs the flow dynamics.

Although magnetic obstacle flows with electrolytes have been less studied than liquid metals flows, interesting patterns and behaviors have been found by different authors (Honji, 1991; Honji and Haraguchi, 1995; Ikehata et al., 1996; Afanasyev and Korabel, 2006b; Afanasyev and Deacon, 2006; Afanasyev, 2006; Afanasyev and Korabel, 2006a; Cruz et al., 2010; Beltrán, 2010; Román, 2013). Former studies have noted that the side walls of the duct may have important effects on the flow behavior, however, this effects have not been investigated deeply. In this work, we study experimentally and numerically the flow of an electrolyte past a magnetic obstacle in a narrow channel, with the aim of
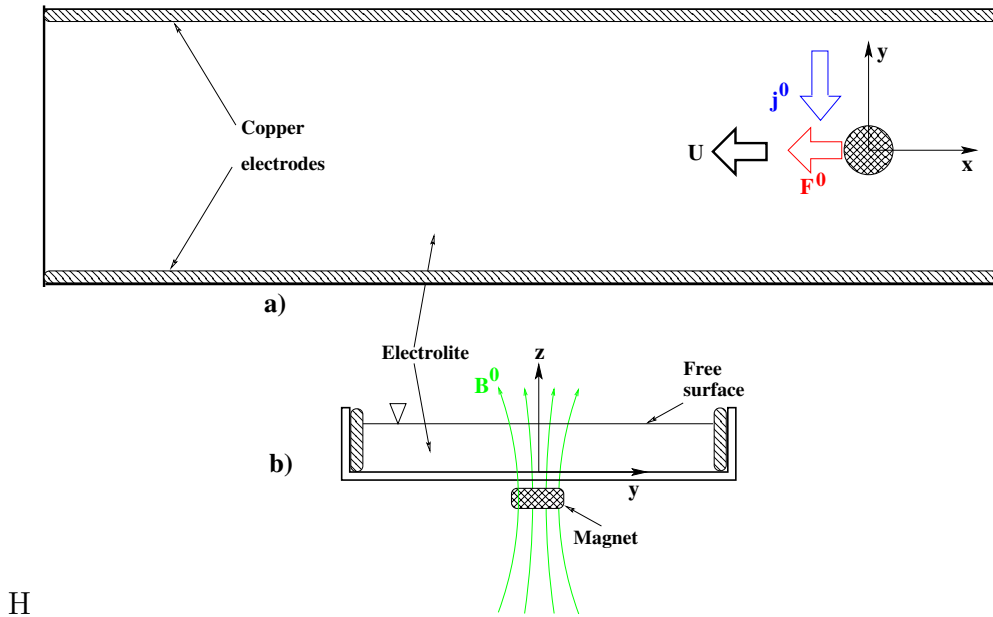
H

Figure 3.1: Sketch of the experimental device, not drawn to scale. (a) Plan view. (b) Cross-section along the y-axis. The velocity of the moving magnet is denoted by U, whereas the imposed electrical current density by j^0 and the main direction of the Lorentz force by F^0. Within the layer, the magnetic field B^0 points mainly in the positive z-direction.

identifying the effect of the blockage parameter on the vortex structures and the vortex shedding behavior in order to get a better understanding of the magnetic obstacle flows that could be of relevance for heat transfer enhancement applications.

3.2 Experimental procedure

In order to widen the range of the explored blockage parameters, two different containers were used. The first container is the one described in Chapter 1, while the second is an acrylic channel with 110 cm long, 10 cm width and 10 cm height. In this channel, copper electrodes were placed along the two sides in the longer direction and connected to a DC voltage power supply. Current intensities in both setups were in the range of 0.01 to 9 A. The channels were partially filled with a weak electrolytic solution of sodium bicarbonate ($NaHCO_3$) at 8.6% by weight. The mass density, kinematic viscosity and electrical conductivity of the electrolyte are $\rho = 1.09 \times 10^3$ Kg/m^3, $\nu = 10^{-6}$ m^2/s, and $\sigma = 6.36$ S/m, respectively. The channels were mounted on supports and level up to get a horizontal layer of water solution with uniform thickness of 0.5 cm. The characteristic length of the flow is controlled by using both channels and magnets of different sizes so that it is possible to vary the blockage parameter. Three different magnets were used for this purpose. The first one is a cylindrical magnet with a diameter of 0.9 cm, a height of 0.5 cm and a maximum strength of 0.21 T. The second magnet is a rectangular parallelepiped

with a side length of 2.54 cm, height of 1.27 cm and maximum strength of 0.33 T. Finally a squared shaped magnet with a side length, height and maximum strength are 5.08 cm, 2.54 cm and 0.33 T, respectively, is used. Magnets were placed beneath the bottom wall of the channel and the maximum strength of magnetic field reported was measured above the bottom wall of the channel. It has to be mentioned that at this location, the shape of the magnet is irrelevant. The magnet is moved along the symmetry axis of the channel with a uniform velocity (see Figure 3.1) using a linear actuator (FESTO EGC-70-500-TB-KF-0H-GK) driven by a servo motor (FESTO EMMS-AS-70-M-RS), in which the velocity of the magnets can be controlled. The velocity of the magnet varied within the range 1.9-111 mm/s. The flow visualization was made by depositing dyed water on top of the free surface. The dye is illuminated in volume using two symmetrically located lamps. As the electrolyte is a transparent medium, the bottom wall was covered with a white sheet for ensuring good contrast in the visualization. The flow was captured with a Nikon D80 camera with a AF micro-nikkor 60 mm f/2.8 D lens.

3.3 Numerical model

The velocity fields of the explored experimental flows were numerically simulated using a quasi-two-dimensional (Q2D) model presented in previous works (Figueroa et al., 2009, 2011; Figueroa, 2010) and adapted to the present problem. This model is based on averaging the balance equations in the normal direction so that flows are described in terms of two-dimensional core variables with a linear friction that accounts for the effects of the boundary layers on the channel walls and the presence of the electromagnetic forces. Within this approximation, only the component of the magnetic field normal to the vertical walls is considered. The decay of the magnetic field in the direction normal to the fluid layer is also considered. In summary, the model can be regarded as a first approach that captures the dominant physical effects without going into the complexities of a full three dimensional model. In contrast with the experiment, the magnet is kept fixed at the origin ($x = 0$, $y = 0$), while a uniform flow at the inlet moves from left to right within the channel in the presence of the braking Lorentz force. However, the latter is consistent with the experimental conditions by using a Galilean transformation. The coordinate system is placed at the bottom wall of the container in such a way that $x - y$ planes remain parallel to this wall and the normal coordinate points in the z-direction. The coordinates are scaled with the side length of the magnet L. The main assumption of the Q2D model is that the transport of momentum in the z-direction is mainly diffusive so that the velocity components can be expressed in the form

$$u(x, y, z, t) = \tilde{u}(x, y, t) f(x, y, z), \quad v(x, y, z, t) = \tilde{v}(x, y, t) f(x, y, z), \qquad (3.1)$$

where $\tilde{u}$ and $\tilde{v}$ are the z-averaged velocity components in the x- and y-directions, respectively. The velocity components in the $x-$ and y-direction, u and v, are normalized by $V = U + u_0$, where U is the velocity of the uniform inlet flow and $u_0 = \nu/L$, ν being the kinematic viscosity of the fluid, respectively. The function f considers the variation of the

velocity profile in the z-direction and must satisfy the normalization condition $\int_0^\varepsilon f dz = 1$, where $\varepsilon = h/L$ is the aspect ratio, h being the layer thickness. The friction function f can be obtained from the following balance between the viscous force, the pressure gradient and the Lorentz force

$$\frac{d^2 f}{dz^2} = Re\frac{\partial P}{\partial x} + \alpha K B_z^0, \tag{3.2}$$

where the pressure field is denoted by P, normalized by ρV^2, where ρ is the density of the fluid. The Reynolds number is defined as $Re = VL/\nu$ and $K = U_0/V$ denotes the ratio of characteristic velocity $U_0 = j^0 B_{max} L^2 / \rho\nu$, obtained from a balance between viscous and Lorentz forces, and the other characteristic velocity V (Figueroa et al., 2009). The normal component of the magnetic field B_z^0 is normalized by the maximum magnetic field strength B_{max}. Due to the decay of the magnetic field in the normal direction, the Lorentz force term in equation (3.2) includes the damping factor α given by (Figueroa et al., 2011)

$$\alpha = \frac{1}{\varepsilon}\int_0^\varepsilon \eta \exp(-\gamma z) dz, \tag{3.3}$$

where $\eta = 1, 1.19, 1.20$ and $\gamma = 2.01, 2.17, 2.11$ are the values obtained from experimental measurements for the three magnets whose characteristic length are 9 mm, 25.4 mm and 50.8 mm, respectively. The f function satisfies the no slip condition at the bottom wall, $f(z = 0) = 0$, and free slip at the free surface, $df(z = h)/dz = 0$. The solution that satisfies the boundary and normalization conditions has the form

$$f = \frac{3\varepsilon\gamma e^{-\gamma z}\left\{2KB_z^0\eta\left(e^{\varepsilon\gamma} + z\gamma e^{z\gamma}\right) - e^{(\varepsilon+z)\gamma}\left(2KB_z^0\eta + Re\frac{\partial P}{\partial x}(z - 2\varepsilon)z\gamma^2\right)\right\}}{3KB_z^0\eta\left(\varepsilon^2\gamma^2 - 2\right) + e^{\varepsilon\gamma}\left(Re\frac{\partial P}{\partial x}\varepsilon^3\gamma^3 + 3KB_z^0\eta(1 - \varepsilon\gamma)\right)}. \tag{3.4}$$

The pressure gradient in eq. (3.4) can be calculated from the mass conservation by evaluating the volumetric flow rate at the channel's entrance (plug flow) and in the zone of developed flow (Poiseuille flow). Thus by equating both volumetric flow rates, the pressure gradient reads

$$\frac{\partial P}{\partial x} = \frac{\frac{12}{Re}\frac{U}{V}}{h^2\left\{1 - \sum_{n,\,odd}^{\infty}\left[\frac{192}{n^5\pi^5}\frac{h}{y}\tanh\left(\frac{n\pi y}{2h}\right)\right]\right\}}. \tag{3.5}$$

In order to obtain the z-average from the conservation equations, we substitute expressions (3.1) and (3.4) into the governing equations and integrate in the z-direction. Dropping the tilde, the dimensionless averaged equations of motion take the form

$$\frac{\partial u}{\partial x} + \frac{\partial v}{\partial y} = 0, \tag{3.6}$$

$$\frac{\partial u}{\partial t} + \zeta \left(u\frac{\partial u}{\partial x} + v\frac{\partial u}{\partial y} \right) = -\frac{\partial P}{\partial x} + \frac{1}{Re} \left(\frac{\partial^2 u}{\partial x^2} + \frac{\partial^2 u}{\partial y^2} \right) + \frac{u}{Re\,\tau} + \alpha Q B_z^0, \quad (3.7)$$

$$\frac{\partial v}{\partial t} + \zeta \left(u\frac{\partial v}{\partial x} + v\frac{\partial v}{\partial y} \right) = -\frac{\partial P}{\partial y} + \frac{1}{Re} \left(\frac{\partial^2 v}{\partial x^2} + \frac{\partial^2 v}{\partial y^2} \right) + \frac{v}{Re\,\tau}, \quad (3.8)$$

where time t is normalized by V/L. The last term on the right-hand side of equation (3.7) considers the Lorentz force created by the non-uniform magnetic field distribution $B_z^0(x,y)$, and the applied electric current density in the negative y-direction, namely, j_y^0 which is normalized by the current density amplitude j^0. Here, B_z^0 is the normal component of the non-uniform magnetic field at a given height z. The dimensionless parameter $Q = j^0 B_{max} L/\rho V^2$ estimates the ratio of the pressure drop due to the electromagnetic force and free stream pressure. Note that both equations (3.7) and (3.8) contain a correction factor ζ in the advective terms, as well as a linear friction term, called Rayleigh friction, which involves a characteristic dimensionless time scale, τ, for the damping of vorticity due to dissipation in the viscous layers at the bottom wall. These parameters are given by

$$\tau^{-1} = \frac{1}{\varepsilon} \int_0^\varepsilon \frac{d^2 f}{dz^2} dz, \quad \zeta = \frac{1}{\varepsilon} \int_0^\varepsilon f^2 dz. \quad (3.9)$$

According to the shallow flow approximation, the aspect ratio $\varepsilon = h/L$ is assumed to be less than unity. In the experiments, the layer depth is constant $h = 5$ mm, therefore, the values of ε are 0.55, 0.2 and 0.1 for the characteristic magnet lengths L equal to 9 mm, 25.4 mm and 50.8 mm, respectively. The system of equations (3.6-3.8), along with the factor α (eq. (3.3)), the 2D distribution of the magnetic field B_z^0, and the friction model (eq. (3.9)), was solved numerically in a rectangular domain using a finite difference code based on Griebel et al. (1998) extended for magnetohydrodynamic flows. The considered boundary conditions are the following.

At the entrance, a uniform flow is imposed in the x-direction, therefore

$$u = 1, \quad v = 0, \qquad \text{at } x = 0, \quad 0 \leq y \leq H. \quad (3.10)$$

At the outlet, Neumann boundary conditions are used, that is,

$$\frac{\partial u}{\partial x} = \frac{\partial v}{\partial x} = 0, \qquad \text{at } x = X_L, \quad 0 \leq y \leq H. \quad (3.11)$$

At the side walls, we use non-slip conditions:

$$u = 0, \quad v = 0, \qquad \text{at } y = 0, H, \quad 0 \leq x \leq X_L. \quad (3.12)$$

Here, H is the dimensionless separation between lateral boundaries defined as

$$H = \frac{X_h}{L}, \quad (3.13)$$

where X_h is the separation between the lateral walls of the channel (in the cross-stream direction). Note that the blockage parameter, β, and H, are related by

$$\beta = \frac{1}{H}. \tag{3.14}$$

Once the Eulerian velocity field is known, the coordinates of passive tracer particles can be found by integrating the (dimensionless) advective equations

$$\frac{dx}{dt} = u(x, y, t), \quad \frac{dy}{dt} = v(x, y, t). \tag{3.15}$$

3.4 Results

The interaction of the moving magnetic field and the electric current generates a traveling localized Lorenz force that tends to produce a vortex dipole, that is, two counter-rotating vortices with a central jet in the negative $x-$direction. The predominance of this structure depends on the flow conditions. As it has been previously stated (Honji and Haraguchi, 1995; Román et al., 2017), depending on the value of the control parameters Re and Q, three flow patterns can be distinguished when the localized Lorentz force acts on the fluid at rest: an open-streamline flow, a vortex pair and a vortex shedding flow. However, by adjusting the distance H between the lateral walls, and consequently the blockage parameter, the three flow patterns can be achieved for the same set of values of the control parameters Re and Q, as is observed in Figure 3.2. This figure shows experimental flow patterns visualized with dye for different values of the blockage parameter β, keeping $Re = 100$ and $Q = 6$. As the parameter β is larger, the effect of the lateral wall is more important. Figure 3.2a) shows a classical (unbounded) BvK wake ($\beta \to 0$), whereas Figure 3.2b) presents the effect of a slight confinement in the wake ($\beta = 1/11$). The presence of the wall constraints the flow to a square-like wake structure, with oval-shaped vortices where the longer shaft is transversal to the stream direction while the center of the vortices moves away from the wall, becoming aligned with the symmetry axis of the channel. Although the walls have an important effect, the wake still presents a BvK structure. When the blockage parameter increases to $\beta = 1/4$, the wall friction brings stability to the flow and delays the transition to the unsteady wake regime, (see figure 3.3c) giving rise to a vortex pair flow pattern. When the blockage parameter increases to $\beta = 1/2$, an open-streamline flow is observed (see figure 3.2d).

Figure 3.3 shows experimental visualizations with their corresponding numerical simulations for two different values of the blockage parameter, namely, $\beta = 1/4$ for figures 3.3a) and 3.3b), and $\beta = 1/2$ for figures 3.3c) and 3.3d). In both cases, a classical BvK wake is found although the strong interaction with the walls causes marked deformations in the wakes. In figures 3.3a) and 3.3b) ($\beta = 1/4$), the centers of the alternated vortices approach closer to the center line of the channel ($x-$axis) than in the case of unbounded flow (see figure 3.2a)). As the the blockage parameter is larger, $i.\ e.\ \beta = 1/2$, the deformation of the vortices is even stronger observing not-well defined shapes in the wake
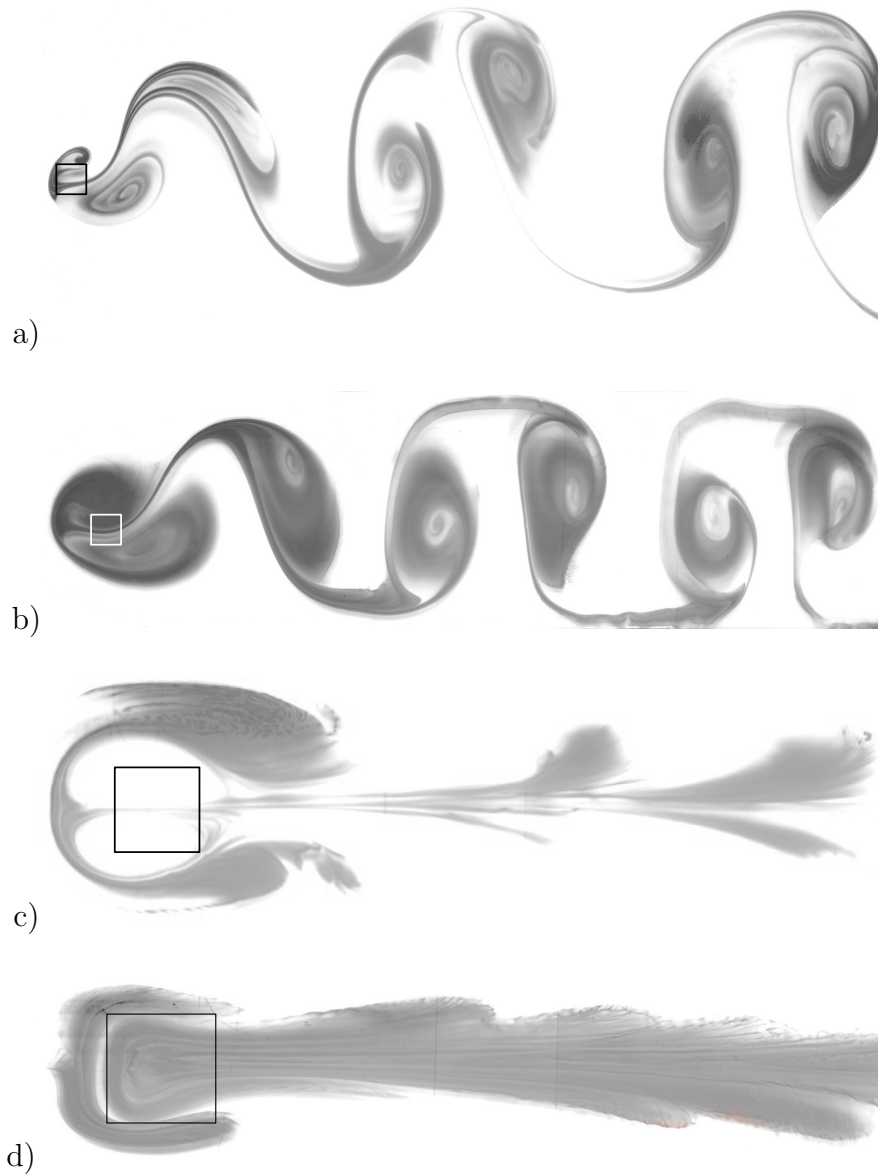
Figure 3.2: Experimental visualization of the flow patterns generated by the moving magnetic obstacle as a function of the blockage paremeter β. The squares denote the footprint of the magnets. a) $\beta \to 0$. b) $\beta = 1/11$. c) $\beta = 1/4$. d) $\beta = 1/2$. $Re = 100, Q = 6$.

as a result of an intense interaction with the walls. In fact, this interaction induces a downstream jet-like flow close to the wall. This flow generates opposite sign vorticity which promotes the downstream displacement of the vortices towards the center line of the channel. Notice also that the larger the size of the permanent magnet the larger the vortices in the wake and the stronger the interaction with the walls. This interaction deeply modifies the structure of the vortex streets. In general, the numerical simulations agree qualitatively with the experimental observations.

Figure 3.4 shows the flow transition maps as function of the parameters Re and Q, for the explored values of the blockage parameter. The left and right panels of this figure correspond to numerical and experimental results, respectively, while each row corresponds to one of the explored values of the blockage parameter, that is, $\beta \to 0$, 1/11, 1/4, and 1/2. For blockage parameter values of $\beta = 1/4$ and 1/2, three zones, separated by continuous lines in figures 3.4c) and 3.4d), are clearly identified. In these two cases, for a fixed Re the transition goes from a jet-like flow to a traveling dipole vortex and finally, to a vortex shedding flow, as the parameter Q increases. Note that when the blockage parameter increases from 1/4 to 1/2, the zone where the traveling dipole vortex appears becomes larger. This means that as the lateral walls are closer, the traveling dipole vortex is more stable. Note also that this zone decreases as Re grows, that is, as the inertial effects increase. For blockage parameters $\beta \leq 1/11$, only two zones concerning the jet-like flow and vortex shedding flow are present (see figures 3.4a) and 3.4b). Note that as β is larger a higher value of Q is required to observe the vortex shedding. On the other hand, as the blockage parameter is also reduced, the value of Q required to promote a vortex shedding flow is reduced. In general, numerical results agree quantitatively with the available experimental results. The agreement is better for larger values of the blockage parameter (1/4 and 1/2) since in these conditions the flow approaches better to quasi-two-dimensionality. In contrast, as β is reduced three-dimensional effects seem to be stronger. We must note that two patterns not observed experimentally were found through numerical simulation, namely, a wall-bouncing vortex pair with $\beta = 1/4$ and a wavy-streamlined flow with $\beta = 1/11$ (see figures 3.4b) and 3.4c). It must be mentioned that in a numerical study of the flow past a solid obstacle for $Re = 100$ and $\beta = 1/2$ reported in the literature (Singha and Sinhamahapatra, 2010) as well as in an experimental study for $Re \leq 108$ and $\beta = 1/3$ (Rehimi et al., 2008), the flow is stable. Evidently, the possibility of varying the strength of the Lorentz forces introduces an additional degree of freedom that allows to modify the relation between inertia and (the magnetic) braking effect. It appears that in the flow past a solid obstacle in the previous cases, walls do not allow the development of instabilities in the recirculation zone behind the obstacle due to the increased friction.

3.5   Conclusions

In this Chapter, we analyzed the effect of the blockage parameter on wake patterns created by a traveling magnetic obstacle in a narrow channel. This parameter, that relates the characteristic length of the magnet that produces the magnetic obstacle with the separation of the lateral walls, was varied by using two different channels and three magnets
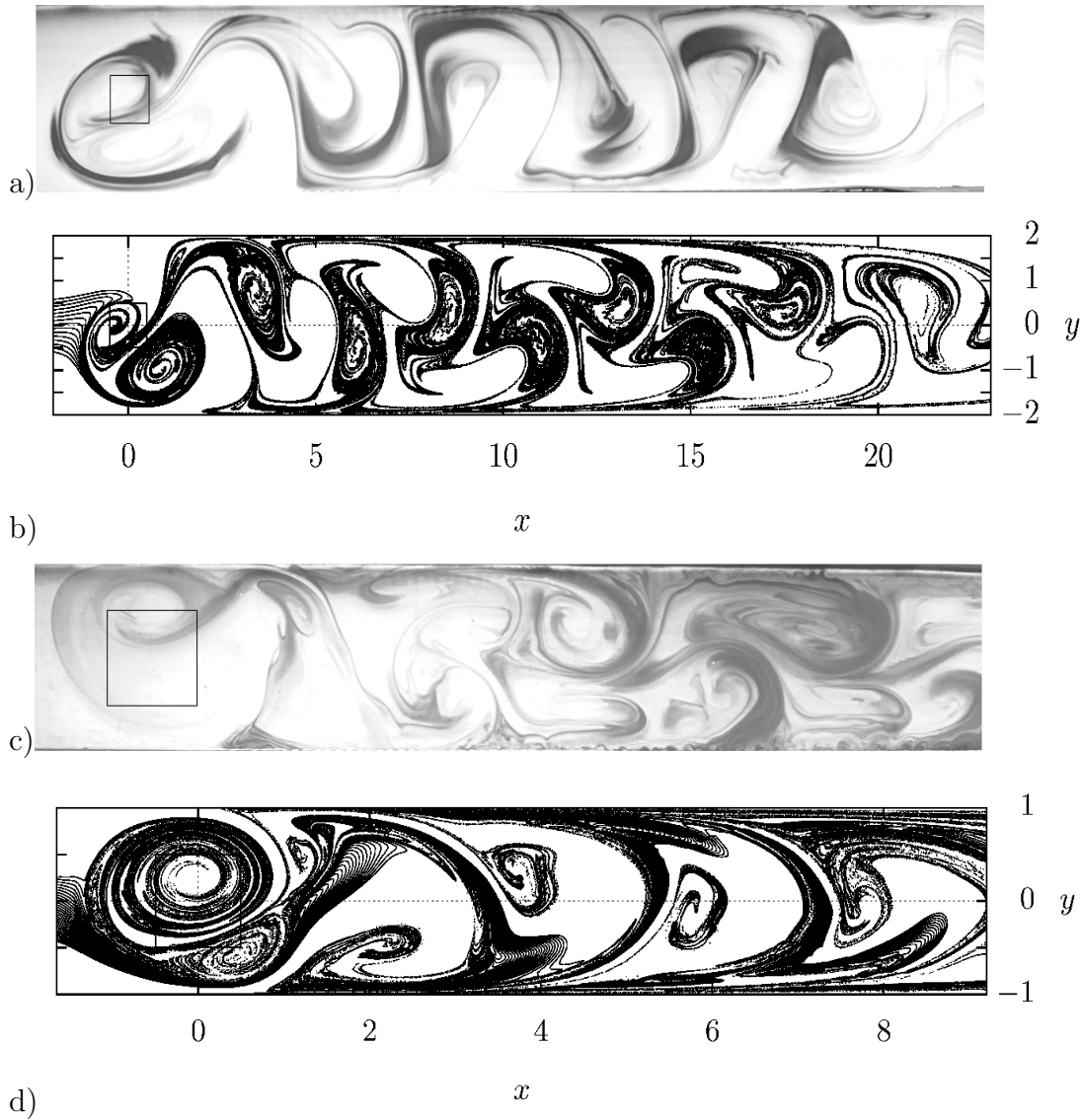
a)

b)

c)

d)

Figure 3.3: Comparison of numerical simulation and experimental visualization of flows produced by a traveling magnetic obstacle. The squares denote the footprint of the magnets. a) and b) $\beta = 1/4$, $Re = 250$, $Q = 8$. c) and d) $\beta = 1/2$, $Re = 250$, $Q = 45$. a) and c) experimental visualization. b) and d) numerical simulations.
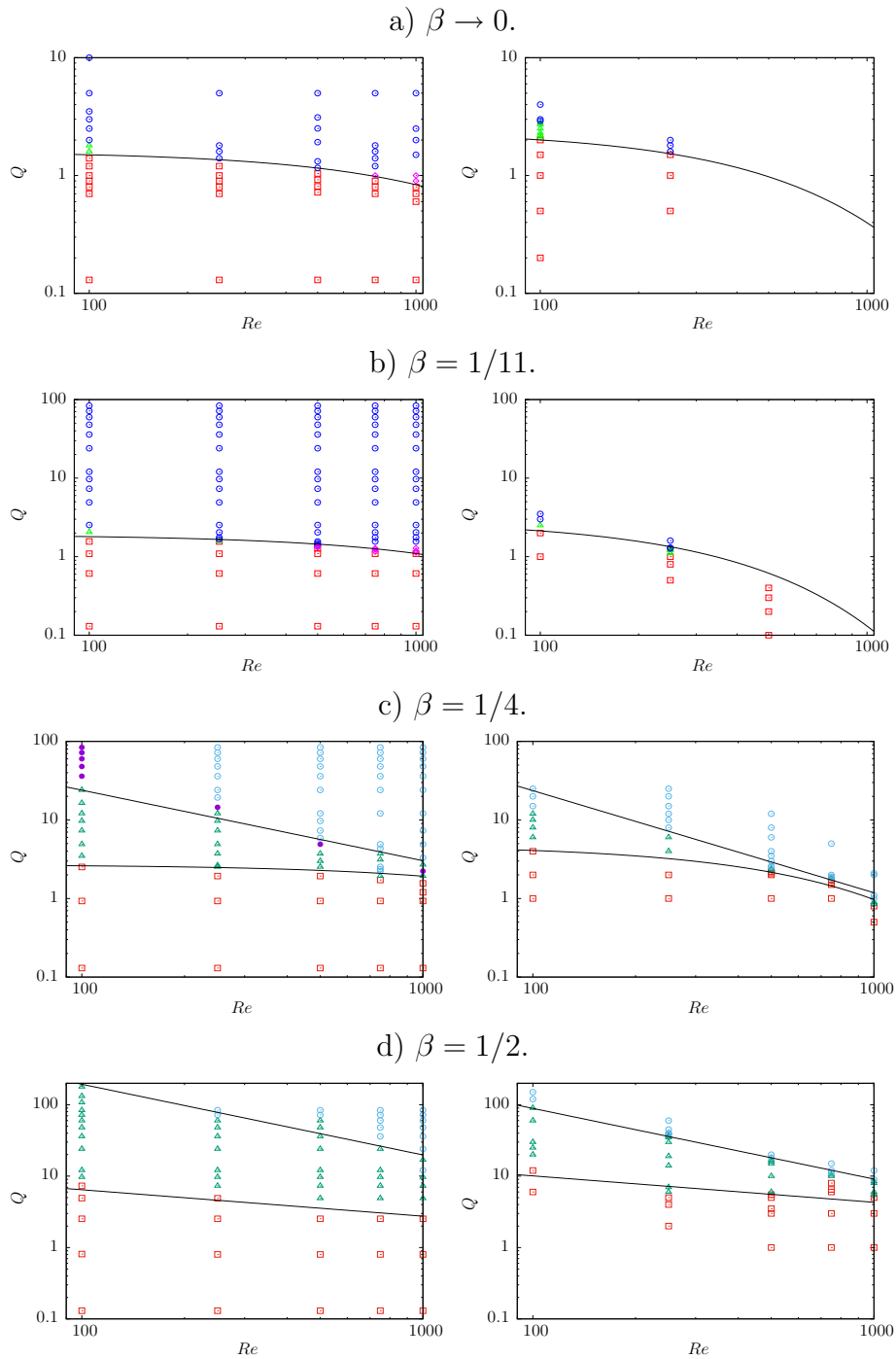
Figure 3.4:   Flow transition maps.   Left column: Numerical results.   Right column: Experimental results. The square ⊡ denotes the jet-like flow. The triangle △ denotes the traveling dipole vortex. The circle ⊙ denotes the vortex shedding flow. The filled circle ● denotes the wall-bouncing vortex pair. The rhomb ◇ denotes the wavy-streamline flow.

of different sizes. Through visualization of the flow using dye the effects of the walls separation on the wake patterns were clearly observed. It was found that as the blockage parameter increases the flow recovers stability in such a way that the flow pattern changes from a Benárd-von-Kármán wake to a traveling dipole and a jet-like flow. Experimental and numerical maps of qualitative flow behavior as function of the governing parameters Re and Q for different values of the blockage parameter show a good agreement in the description of the flow transitions among the observed wake patterns. It is interesting to note that when the blockage parameter increases a higher value of Q is required to get the vortex shedding which indicates that a stronger electromagnetic force is required to destabilize the flow when the effect of the wall friction becomes more intense. Although the simplified quasi-two-dimensional numerical model correctly captures the main physical effects of this flow, numerical results display a better agreement with experimental results for larger values of the blockage parameter for which the flow approaches better the quasi-two dimensional behavior.

Experimental and theoretical study of wake patterns behind a magnetic obstacle in a liquid metal flow

In this Chapter[1], we present an experimental and theoretical study of the dynamics of wakes generated by magnetic obstacles. The experimental magnetic obstacle was realized by circulating a liquid metal inside a closed loop with a slender cross-section and imposing a fixed localized magnetic field in a specific spot of the loop. Experimental observations made with an Ultrasonic Doppler Velocimeter include records of the axial velocity of liquid metal as a function of the axial coordinate in the region where the wake of the obstacle is formed. This information reveals important features of the stability and dynamics of the wake of the magnetic obstacle. The theoretical study is based on a numerical solution of a quasi-two dimensional model of the MHD balance equations whose non-dimensional form indicates that the flow can be described in terms of two parameters, the Reynolds and the Hartmann numbers. The numerical model considers the induced magnetic field as an electromagnetic variable (B-formulation). Theoretical studies predict that for a given Hartmann number, the flow transits from a steady state to a time-dependent state as the Reynolds number is increased as occurs in the wake of a rigid obstacle, but in sharp contrast to this last case, when the Reynolds number is increased further, the flow becomes steady again. Our experimental observations confirm that this prediction is correct.

4.1   Introduction

The term magnetic obstacle is used to denote the braking Lorentz force that opposes the flow of an electrically conducting fluid due to the presence of a localized magnetic field. The relative motion between the fluid and the applied magnetic field induces electric currents that interact with the field and generate a localized Lorentz force that acts as an obstacle for the flow. In the 1970's, it was realized that complex velocity structures could appear in flows under non-uniform magnetic fields (Gelfgat et al., 1978), although experimental results were not able to confirm this fact (Gelfgat and Olshanskii, 1978). In the

---

[1]This Chapter is mainly based on the paper: Domínguez, D. R., Beltrán, A., Román, J., Cuevas, S., and Ramos, E. "Experimental and theoretical study of the dynamics of wakes generated by magnetic obstacles." *Magnetohydrodynamics*, **51**, 215-224 (2015).

last decade, several studies (mainly theoretical) have explored the flow past magnetic obstacles and described important physical features (Cuevas et al., 2006a,b; Votyakov et al., 2007, 2008; Votyakov and Kassinos, 2009, 2010; Kenjeres et al., 2011; Tympel et al., 2013; Andreev et al., 2009; Ramos et al., 2008). The first studies used a numerical approach to provide a quasi-two-dimensional description of the flow in conditions where inertial effects were not negligible (Cuevas et al., 2006a), and under creeping flow conditions (Cuevas et al., 2006b). It was shown that both time-dependent and steady vortical flows that in some aspects resemble flows past bluff bodies, may appear. Through numerical simulation and experiments, other studies revealed that a steady six-vortex pattern that is not observed in hydrodynamic flows could appear in the wake of a magnetic obstacle at certain values of the Reynolds number Re, interaction parameter N (or equivalently the Hartmann number Ha) and constrainment factor κ defined as the ratio of the lateral size of the magnet exposed to the oncoming flow to the width of the channel (Votyakov et al., 2007, 2008). The analogy between flows past solid and magnetic obstacles has been investigated, recognizing that important differences exist between these two physical situations (Votyakov and Kassinos, 2009, 2010). Other numerical simulation studies have shown that the imposition of magnetic fields of different strengths may give rise to transitional flow regimes for a fixed Re and different values of the interaction parameter, observing vortex shedding phenomena as well as sustained turbulent bursts close to the magnetic wake region (Kenjeres et al., 2011). Recently, the influence of a localized non-uniform magnetic field on liquid metal flow in the quasi-static approximation was investigated numerically (Tympel et al., 2013). These authors analyzed the three-dimensional flow transformation and the generation of vortex structures by a strong magnetic dipole field in a liquid metal duct flow. An important feature of the wakes generated by magnetic obstacles, detected with the ultrasonic velocity profile method, is that the length of the recirculation region behind the magnetic obstacle increases with the Reynolds number to reach a maximum and then decreases (Andreev et al., 2009). Preliminary, theoretical studies indicate that for large enough Hartmann numbers, increasing the Reynolds number results in the formation of a wake behind the magnetic obstacle with a characteristics, similar to a Bénard von-Kármán vortex street that occurs behind a rigid obstacle, but in sharp contrast to the dynamic behavior of the wake formed by a rigid obstacle a further increase of the Reynolds number leads to a reduction of vortex shedding behind the magnetic obstacle (Ramos et al., 2008). In the present contribution, we extend the study presented in (Ramos et al., 2008) by describing the experimental recordings that were made to detect the axial velocity of the flow of liquid metal in the presence of a magnetic obstacle with the objective of determining representative properties of the wake. The observations show that for a fixed Hartmann number, the energy contained in the vortices of the wake does present a maximum as a function of the Reynolds number, indicating that the obstacle sheds vorticity to the ambient in a finite range of Reynolds numbers. Using a numerical solution, we infer the dynamics of the whole structure of the wake.

4.2 Experimental set up

The experimental device used in the observations is a rectangular loop made from acrylic (Polymethyl methacrylate) walls with a rectangular effective cross-section of 1 cm × 8 cm. The lengths of the large and short legs of the duct are 85.8 cm and 40 cm, respectively. The loop is built in sections joined with flanges and the whole system is fixed with mounts that separate it from the floor of the table, making it easier to detect possible leaks. By straddling one of the long legs at the central region, an MHD induction pump with rotating permanent magnets is located. The pump consists of a motor that spins two disks, where 24 permanent neodymium magnets are mounted radially; this device sets the liquid metal in motion around the loop. The velocity of the liquid metal is measured by a Signal Processing ultrasonic Doppler velocimeter (UDV) using a probe of 0.8 cm in diameter and a wave frequency of 4 MHz. With this equipment, it is possible to determine one component of the velocity along the propagation line of the acoustic wave emerging from the emitter. The ultrasonic gauge was fixed at the downstream end of the region of analysis to detect the axial velocity along the axial coordinate. An appropriate mount was used to place the gauge at different vertical positions. The flow generated by the pump is characterized using the Reynolds number defined as $Re = UL/\nu$, where U is the average axial velocity, L is the hydraulic diameter of the cross-section and ν is the kinematic viscosity of the working fluid (see below). Given that the geometry of the duct and the physical properties of the fluid are fixed, the range of Reynolds numbers available with the experimental equipment depends on the power delivered by the pump (or equivalently the pressure difference) and on the resistance of the duct. We determined the range of the Reynolds number available through direct measurement of the axial velocity. Our measurements indicated that $869 < Re < 4960$. A photograph of the experimental device indicating the position of the MHD pump, the magnets and the UDV system, is shown in Figure 4.1. The design of our equipment follows closely that of similar facilities developed at the Technical University of Ilmenau, Germany (see, for instance, (Jian and Karcher, 2012) and (Heinicke, 2013)). A sketch showing the position of the magnets and the UDV, together with some details of the flow, and the axes of coordinates used in the numerical study are shown in Figure 4.2.

The working fluid is a Ga(68%)In(20%)Sn(12%) eutectic alloy which has a melting temperature of 10.5°C and a kinematic viscosity of $\nu = 3.3 \times 10^7$ m^2/s. The magnetic obstacle is created by two 2.54 cm × 2.54 cm × 1.25 cm neodymium magnets placed on the outer side of the opposite vertical walls of the central part of one of the long legs. The magnets are located 30 cm away from the upstream corner and 4 cm from the lower horizontal wall of the duct. With this magnet arrangement, the maximum magnetic field that can be obtained at the center of the duct is 0.23 T, and the constrainment factor is $\kappa = 0.31$ (the side of the magnet/height of the duct). A second non dimensional parameter that characterizes the flow is the Hartmann number defined as $Ha = B_0 D \sqrt{\sigma/\rho\nu}$, where B_0 is the maximum strength of the magnetic field at the center of the duct, D is the gap between the vertical walls of the duct, and σ and ρ are the electric conductivity and the density of the working fluid, respectively. For GaInSn, $\sigma = 3.46 \times 10^6$ 1/Ωm and $\rho =$
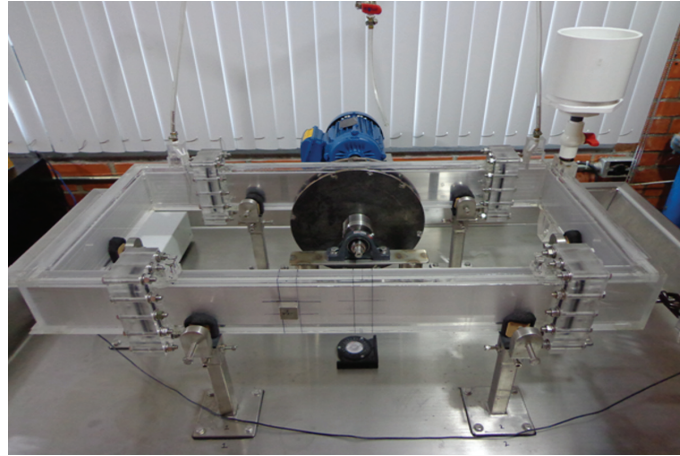
Figure 4.1: The experimental liquid metal loop. The MHD pump is in the far long leg. The disks with permanent magnets and the liquid metal rotate in the counterclockwise direction. The magnet that generates the magnetic obstacle is close to the central part of the near long leg, 30 cm away from the upstream corner and 4 cm above the lower wall of the duct. The ultrasonic gauge is in the far right of the picture near the duct corner.

6360 kg/m^3. The range of Hartmann numbers available depends on the intensity of the permanent magnets used and their relative position with respect to the liquid metal, but increasing the distance of the magnets to the vertical walls reduces the effective magnitude of the magnetic field inside the duct and also reduces the Hartmann number. In figure 4.3, we show the distribution of the normal component of the magnetic field for distances of 3.1cm and 3.6 cm between the magnets. These conditions yield Hartmann numbers of 58 and 75, respectively. As can be appreciated, both magnetic fields have similar to Gaussian distributions, but with different spread and maximum values. As it is usual in liquid metal MHD duct flows, the magnetic Reynolds number defined as $Rm = \mu_0 \sigma U D$ is very small.

4.3 Numerical model

A quasi two-dimensional (Q2D) model is proposed to simulate the MHD flow through a spatially localized magnetic field produced by magnets fixed to the channel walls. This simplified model can be regarded as a first approach that captures the dominant physical effects without going into the complexities of a full three dimensional model. Within this approximation, only the component of the magnetic field normal to the vertical walls is considered. The origin of the axis of coordinates is located on the line that joins the geometrical center of the magnets and the halfway between the vertical walls of the duct (see Figure 4.3). The dimensionless axial (x) and vertical (y) coordinates increase in the downstream and upward directions, respectively, and are scaled with the side length of the magnet L. The traversal coordinate (z) is defined in the direction perpendicular to the vertical walls and scaled by D. The main assumption of the Q2D model is that
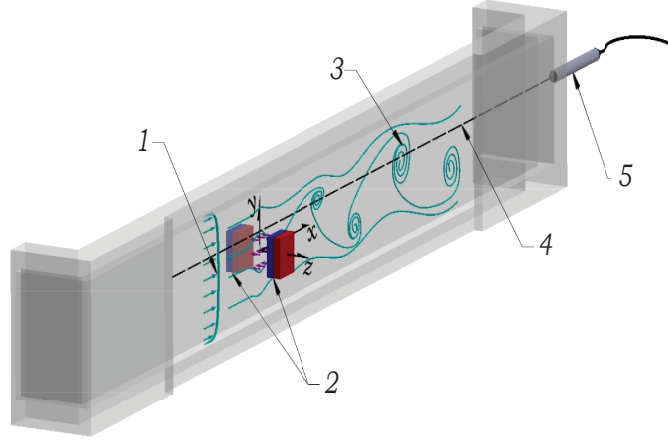
Figure 4.2: Sketch of the observation zone and position of the axis of coordinates. 1 - upstream velocity profile, 2 - magnets, 3 - wake of the magnetic obstacle, 4 - line for ultrasonic Doppler velocity recordings, 5 - ultrasonic Doppler velocimetry probe.

the transport of momentum in the z-direction is mainly diffusive so that the velocity components can be expressed in the form

$$u(x, y, z, t) = \tilde{u}(x, y, t) f(x, y, z), \quad v(x, y, z, t) = \tilde{v}(x, y, t) f(x, y, z), \quad (4.1)$$

where $\tilde{u}$ and $\tilde{v}$ are the z-averaged velocity components in the x- and y-directions, respectively. The velocity components are scaled by the average axial velocity U. The function f considers the variation of the velocity profile in the z-direction and must satisfy the normalization condition $\int_{-1/2}^{1/2} f \, dz = 1$. Its dependence on the x and y coordinates must reflect the different flow regions due to the localization of the magnetic field. Details of the quasi-two dimensional model can be found in Cuevas et al. (2006a). The friction function f can be obtained from the following balance between the viscous and the Lorentz force

$$\frac{\mathrm{d}^2 f}{\mathrm{d}z^2} - (Ha B_z^0(x, y))^2 f = \epsilon^2 Re \frac{\mathrm{d}p}{\mathrm{d}x}, \quad (4.2)$$

where ϵ is the aspect ratio D/L. The terms on the left-hand side correspond to the viscous and induced Lorentz forces, while the term on the right-hand side is an externally imposed axial pressure gradient which generates the duct flow and is constant. It should be noted that due to the normalization for f, this parameter does not appear explicitly in the solution. The function f must satisfy no-slip conditions at both vertical walls $f(z = \pm 1/2) = 0$. The solution that satisfies the boundary and normalization conditions has the form

$$f = -\mathcal{H}a \; \mathrm{e}^{-\mathcal{H}a(z+0.5)} \times \frac{\mathrm{e}^{\mathcal{H}a} - \mathrm{e}^{2\mathcal{H}a} - \mathrm{e}^{\mathcal{H}a(z+0.5)} + \mathrm{e}^{\mathcal{H}a(1+2z)} - \mathrm{e}^{2\mathcal{H}a(1+z)}}{4\mathrm{e}^{\mathcal{H}a} + (1 - \mathrm{e}^{2\mathcal{H}a})(\mathrm{e}^{\mathcal{H}a} + 2)} \quad (4.3)$$
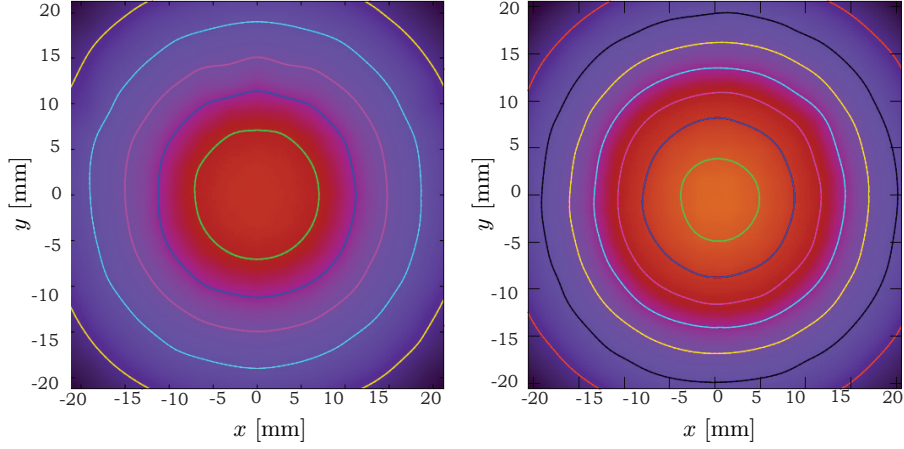
Figure 4.3: Magnetic field distribution at the center of the duct for Hartmann numbers 58 (left) and 75 (right). The central circles represent 0.125 T and 0.175 T for Hartmann numbers 58 and 75, respectively. In the two cases, the contours are 0.025 T separated.

where $\mathcal{H}a = HaB_z^0$ is defined as the local Hartmann number. In order to obtain the z-average from the conservation equations, we substitute expressions (4.1) and (4.3) into the governing MHD equations and integrate in the z-direction. Dropping the tilde, the dimensionless averaged equations of motion take the form

$$\frac{\partial u}{\partial x} + \frac{\partial v}{\partial y} = 0, \tag{4.4}$$

$$\frac{\partial u}{\partial t} + u\frac{\partial u}{\partial x} + v\frac{\partial u}{\partial y} = -\frac{\partial P}{\partial x} + \frac{1}{Re}\nabla_\perp^2 u + \frac{u}{\tau} + \frac{Ha^2}{\epsilon^2 Re}j_y B_z^0, \tag{4.5}$$

$$\frac{\partial v}{\partial t} + u\frac{\partial v}{\partial x} + v\frac{\partial v}{\partial y} = -\frac{\partial P}{\partial y} + \frac{1}{Re}\nabla_\perp^2 v + \frac{v}{\tau} - \frac{Ha^2}{\epsilon^2 Re}j_x B_z^0, \tag{4.6}$$

where the pressure p, the electric current density components j_x and j_y, and the applied field $B_z^0(x,y)$ are scaled by ρU^2, $\sigma U B_0$, and B_0, respectively. The sub index $\perp$ denotes the projection of the nabla operator on the (x,y)-plane. The time t is normalized by L/U. The model shows that there are two nondimensional parameters, the Reynolds (Re) and the Hartmann (Ha) number (for definitions see Section 4.2). The third term on the right-hand side of Eqs. (4.5) and (4.6) represents the Hartmann-Rayleigh friction and arises due to the boundary layers at the Hartmann walls. The Hartmann-Rayleigh friction can be conveniently represented in terms of a characteristic dimensionless timescale τ, which indicates the decay of vorticity due to dissipation in the Hartmann and viscous layers. The inverse of this time scale is given by

$$\tau^{-1} = \frac{1}{\epsilon^2 Re}\left.\frac{\mathrm{d}f}{\mathrm{d}z}\right|_{-1/2}^{1/2} = -\frac{1}{\epsilon^2 Re}\frac{2\mathcal{H}a^2(\mathrm{e}^{\mathcal{H}a}+1)^2}{4\mathrm{e}^{\mathcal{H}a} + (1-\mathrm{e}^{2\mathcal{H}a})(\mathcal{H}a+2)}. \tag{4.7}$$

In the quasi-static approximation the magnetic induction equation takes the form

$$\nabla_\perp^2 b_z - u\frac{\partial B_z^0}{\partial x} - v\frac{\partial B_z^0}{\partial y} = 0, \tag{4.8}$$

where the induced magnetic field b_z has been normalized by RmB_0. Once b_z is determined, the Ampere's law gives an expression to calculate electric currents, namely,

$$j_x = \frac{\partial b_z}{\partial y}, \quad j_y = -\frac{\partial b_z}{\partial x}, \tag{4.9}$$

A solution to the quasi two-dimensional model given in Eqs. (4.4)-(4.9) is sought via numerical methods. The finite volume method described in Versteeg and Malalasekera (1995) on an orthogonal equidistant grid was used to solve the conservation equations (4.4)-(4.8). The distribution of the applied magnetic field $B_z^0(x,y)$ required for the numerical solution is a fit of the experimental magnetic field (Figure 4.3) with the expression given by McCaig (1977) for a square surface magnetized in the normal direction. The numerical solution was obtained in a rectangular domain of 35×3.2 non-dimensional units using a grid of 700×256. The boundary conditions consider no-slip conditions for the velocity components at $y = \pm 1.6$. At the inlet ($x = -10$), a uniform velocity profile is used, whereas Neumann boundary conditions are imposed at the outlet ($x = 25$). We assume that the induced magnetic field is zero $b_z = 0$ at all boundaries. The standard time marching procedure (Euler method) was used for the time integration with a non-dimensional time step of 5×10^{-4}.

4.4 Results

Exploratory observations indicate that the flow generated by the magnetic obstacle is a very complex, three dimensional, time dependent phenomenon, whose comprehensive description would require a large research program. In the present study, we concentrate on a very specific aspect of this flow, namely, in the detection of vortical structures in the wake as functions of the Reynolds number. Before we present quantitative results, it is convenient to describe some qualitative features of the flow. The axial velocity u in the (x,t) space and for the vertical position $y = 12.7$ mm is plotted in figure 4.4. The left panel displays the experimental recordings obtained with UDV for $Ha = 75$ and $Re = 2300$, and the right panel shows similar results obtained with the numerical solution using $Ha = 80$ and $Re = 2500$. A zoom is provided for the experimental results. An interesting feature of the experimental records is that the axial velocity just upstream the magnetic obstacle is reduced (red-purple vertical strip at -50 mm $< x <$ 0 mm) and then it increases in the region 0 mm$< x <$140 mm. The inclined, red and purple parallel strips in the region $x > 170$ mm indicate the transit of a periodic perturbation in time for a fixed point in space, or in space for a snapshot. This velocity pattern is consistent with vortex shedding with an approximate characteristic time of the order of 1.0 s. The results obtained with

the numerical solution display similar features, with periodic inclined parallel strips that indicate the transit of periodic structures.
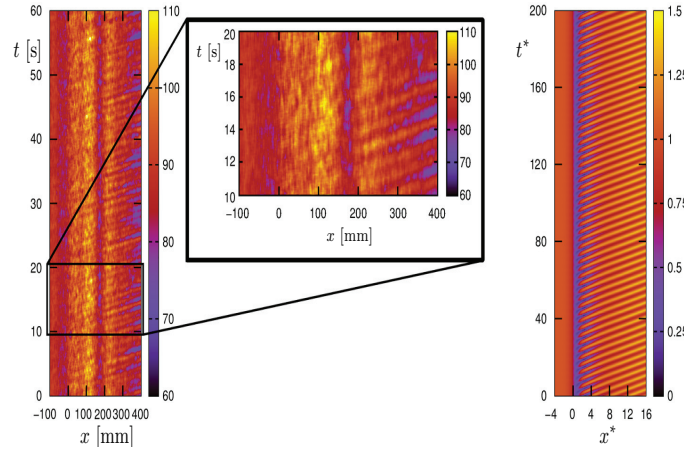

Figure 4.4: Map of the axial velocity u in the (x, t) space, $y = 12.7$ mm. Left: experimental observations for $Ha = 75$, $Re = 2300$. Right: numerical calculation for $Ha = 80$, $Re = 2500$.
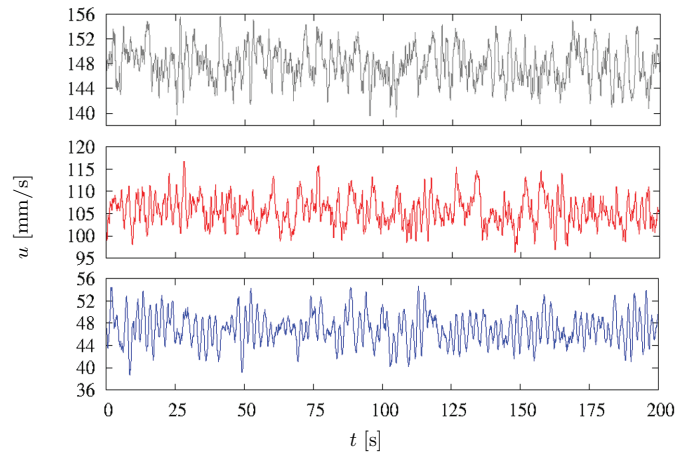

Figure 4.5: Experimental axial velocity u as a function of time at the point $x = 400$ mm, $y = 12.7$ mm for $Ha = 75$. Starting from the top, traces were obtained for $Re = 1272, 3163$ and 4568. Note the different scales in the ordinates of the three graphs and that the largest amplitude corresponds to $Re = 3163$.

In order to a make a more specific analysis, we show in Figure 4.5 a sample of the axial velocity traces observed at a fixed point ($x = 400$ mm, $y = 12.7$ mm) as a function of time for $Ha = 75$ and $Re = 1272$, 3163 and 4568. The sampling frequency was $20 Hz$. The original traces were smoothed with a moving average filter of 15 points, equivalent to a sampling rate of 0.75 s. As seen, the traces are irregular, with many Fourier modes involved, and also the average amplitude of the perturbations is not a monotonous function of the Reynolds number. Note that the time average of the signals increases

with the Reynolds number, as expected, but in contrast, we find that the amplitude of the velocity fluctuations is larger for the case $Re=3163$ than for of the other two cases in Figure 4.5. With the velocity traces alone, it is difficult to quantify the amplitude difference between the different cases and, in the following, we will develop methods to obtain a more quantitative assessment. The average velocity obtained by experimental and numerical methods is of the same order of magnitude, indicating that this feature is correctly captured with the model. However, the oscillations superimposed to the average flow calculated numerically have single or few Fourier modes, with periods of approximately 3.7 non-dimensional units. See also the right panel of Figure 4.4. An alternative way of displaying the previous results that is more amenable for comparison is to plot the parameter $\mathcal{A}$ defined by

$$\mathcal{A} = u - \langle u \rangle, \tag{4.10}$$

where $\langle u \rangle$ is the average axial velocity over a time interval I_0. In Figure 4.6, we show 40s of the readings of the variable $\mathcal{A}$ as a function of time for the same Reynolds numbers analyzed in Figure 4.5 and using $I_0 = 53$s (103 readings). Inspection indicates that the amplitude of the traces is of the order of 10 mm/s and that the amplitude of the perturbations obtained with $Re = 3163$ is larger than that found in the other cases. The corresponding properties of the flow obtained with numerical integration show that the amplitude of the oscillation is much smaller (of the order of 0 ± 25 mm/s), which is by a factor of 20 smaller than the observed experimental value.
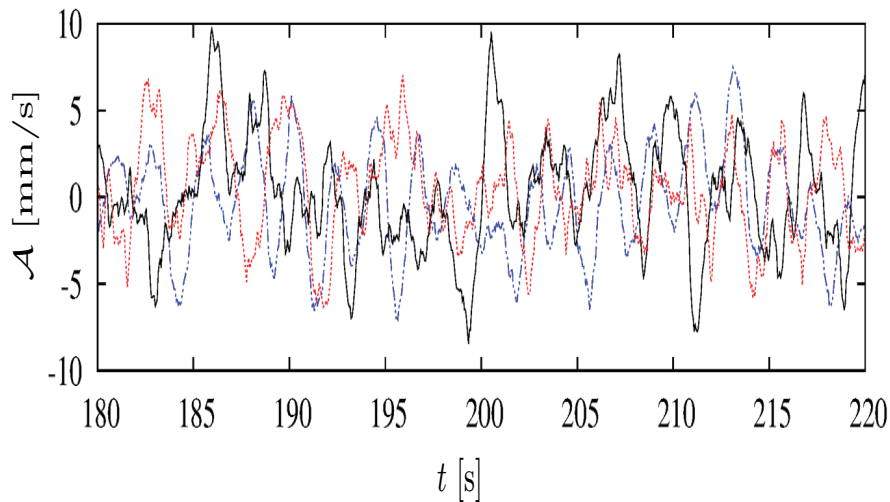

Figure 4.6: The parameter $\mathcal{A}$ as a function of time for three Reynolds numbers: $Re = 1272$ (blue line-dots), 3163 (black continuous line) and 4568 (red dots).

In order to make a quantitative comparison, we define the parameter $\mathcal{L}^2$ as

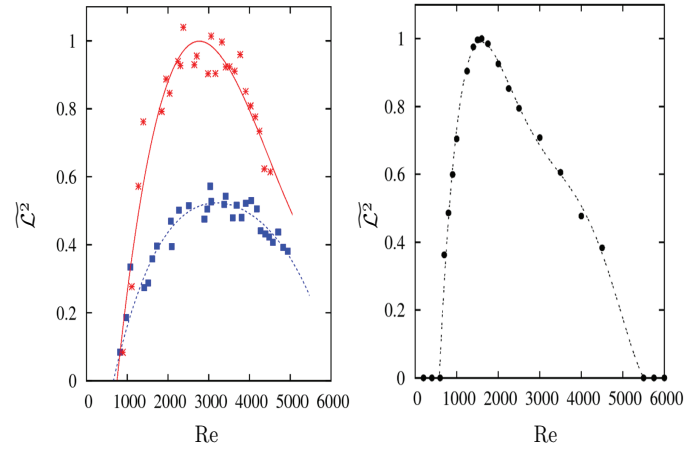$$\mathcal{L}^2 = \frac{1}{I} \int_0^I \mathcal{A}^2 \, \mathrm{d}t. \tag{4.11}$$

Figure 4.7: The parameter $\mathcal{L}^2$ as a function of the Reynolds number. Left panel: experimental observations. $Ha = 58$ (blue line with squares) and $Ha = 75$ (red line with asterisks). The lines are fits to the experimental data. The fits of $\widetilde{\mathcal{L}^2}$ attain maxima at Re = 3190 and 2750 for $Ha = 58$ and 75, respectively. Right panel: theoretical calculations. $Ha = 80$, the maximum is attained at approximately $Re = 600$.

Note that $\mathcal{L}^2$ is a function of the Hartmann and Reynolds numbers only and indicates the average of the square of the amplitude of the axial velocity oscillation with respect to its average value in the interval I which is related to the kinetic energy of the vortices in the wake.

In the left panel of Figure 4.7 we show the experimental results for $\mathcal{L}^2$ at $Ha = 58$ and 75 as functions of the Reynolds number. The actual data shown in the figure and denoted by $\widetilde{\mathcal{L}^2}$ are normalized with the maximum (smoothed) value of $\mathcal{L}^2$ ($Ha = 75$). As it can be seen from the figure, the trends of $\widetilde{\mathcal{L}^2}$ are not monotonous but display maxima. Our experimental device allows us to capture data for very small values, which leads us to determine the critical Reynolds number, where the first bifurcation occurs, i.e. where the wake of the magnetic obstacle becomes time dependent; $\widetilde{\mathcal{L}^2}$ is zero for Reynolds numbers smaller than the critical ones. The first critical Reynolds number is found at approximately 900 for the two cases explored. The experimental equipment prevents us to obtain data for Reynolds numbers larger than approximately 5000 for $Ha = 58$ and 75, but in the two cases, the data display an unmistakeable trend towards smaller values. Extrapolating the experimental data available, the Reynolds number where $\widetilde{\mathcal{L}^2}$ reduces to zero, is approximately 6000 for $Ha = 75$, but for $Ha = 58$ it is difficult to estimate the Reynolds number, where the energy of the perturbations in the wake vanishes. The maxima of the smoothed data are attained at $Re = 3190$ and 2750, respectively, for $Ha = 58$ and 75. The trend displayed by $\widetilde{\mathcal{L}^2}$ obtained with the numerical solution and considering $Ha = 80$ is shown in the right panel of Figure 4.7. The data have been normalized with its maximum value. The variable $\widetilde{\mathcal{L}^2}$ obtained by numerical calculations displays qualitative features similar to those observed in the experiment, and the range of Reynolds numbers where the wake of the obstacle sheds vortices, is approximately the

same for theory and experiment, but the amplitude is not. The latter is a consequence of the fact that the model underestimates the amplitude of the velocity fluctuations, as indicated in the discussion of Figure 4.6.

4.5 Conclusions

Experimental records of the wake formed by a magnetic obstacle in a liquid metal flow made by an ultrasonic velocimeter are presented. The velocity readings show intermittent perturbations that indicate vortex shedding from the magnetic obstacle. We observe that for small Reynolds numbers ($300 < Re < 700$) the energy of the perturbations in the wake increases to reach a maximum that depends on the Hartmann number. Then the energy reduces monotonically up to the maximum Reynolds number that can be reached with our experimental equipment. This indicates that the oscillatory wake is present in the flow only in a finite range of Reynolds numbers. This observation is in qualitative agreement with a quasi-two-dimensional theory also presented in this report. Although a more detailed study of the behavior near the first critical Reynolds number, where the steady flow becomes time dependent is required, the data available evidence that the first bifurcation is a supercritical Hopf bifurcation (for a definition see Lynch (2004)). The first critical Reynolds number detected is much larger than the rigid cylindrical obstacle (approximately 45 (Williamson, 1996)); this effect may be due to the stabilizing effect of the lateral walls. Unfortunately, our experimental equipment prevents us to explore the nature of the inverse bifurcation found at large Reynolds numbers, but the numerical solution suggests that it is an inverse supercritical Hopf bifurcation. The numerical model used to simulate the specific feature of the flow analyzed in this contribution does capture the magnitude of the average velocity correctly, but fails to give good results on the complexity and magnitude of the velocity fluctuations.

Experimental study of wake patterns behind a solid disk

In this Chapter[1], we study experimentally a flow past a circular disk immersed in a water channel at high Reynolds numbers. The disk is located at the center of the channel so that its symmetry axis is aligned with the direction to the flow. Using a rear view configuration in which the laser sheet is perpendicular to the direction of the flow, we analyze the flow pattern using Particle Image Velocimetry. Measurements were made with Reynolds numbers in the range from 250 to 550, where oscillatory instabilities appear. In order to obtain a more detailed description of the flow, an azimuthal Fourier decomposition was performed using an algorithm implemented in a MATLAB code. The Fourier decomposition allow us to reconstruct the azimuthal modes of the original vorticity field. It was found that the temporal evolution of the longitudinal component of the vorticity, shows an instability that may have a long-term frequency.

5.1   Introduction

As we have already mentioned, the flow past solid obstacles and the wake patterns generated behind them, have been extensively studied in the literature (Zdravkovich, 1997). Within this topic, an interesting and important phenomenon is the study of the vortex shedding behind three-dimensional bluff bodies, for example a sphere, a disk or a cube.

In fact, one of the subjects of interest of the research group led by Dr. Wesfreid at PMMH-ESPCI (Bobinski et al., 2014; Gumowski et al., 2008; Klotz et al., 2014) is the study of vortex shedding behind axisymmetric solid obstacles as those just mentioned in which three dimensional wake structures can be identified (Bobinski et al., 2014). For instance, in the flow behind a sphere, three different flow regimes have been reported. For $Re < 212$, the wake of the sphere has an axisymmetric stationary ring structure. At $Re = 212$ two parallel and counter-rotating vortices appear. The transition between a steady structure and a time dependent structure occurs at $Re = 275$ (Gumowski et al., 2008). This flow pattern is known as the hairpin vortex shedding where small pieces of counter-rotating

---

[1]This Chapter is mainly based on the results obtained during the internship at PMMH-EPSCI (Physique et Mécanique des Milieux Hétérogènes-École de Physique et de Chimie Industrielles) of Paris-Tech in Paris, France, under the supervision of Dr. Ramiro Godoy-Diana, Dra. Sophie Goujon-Durand and Dr. José Eduardo Wesfreid.

vortices are produced by stages of strong modulation and reconnection of two marginal longitudinal vortices (Gumowski et al., 2008). The flow structures generated behind a disk have also been investigated experimentally, observing the same three flow patterns found in the flow past the sphere. The first observed pattern is a steady axisymmetric flow with a toroidal recirculation zone behind the disk. By increasing the Reynolds number the toroidal recirculation zone becomes a non-axisymmetric structure formed by two counter-rotating vortices. By increasing the Reynolds number the flow structure is transformed giving rise to the hairpin vortex shedding (Bobinski et al., 2014). It has been observed that the value of the Reynolds number at which the transition of the steady flow pattern to the one where vortices appear varies according to the thickness of the disk. For a very thin disk the transition between the flow patterns occurs at higher Reynolds numbers (Bobinski et al., 2014). Figures 5.1 shows the experimental patterns for the flow past a circular disk (Klotz et al., 2014). In turn, figure 5.2 shows flow patterns for the flow past a cube where a close resemblance with the patterns found with the sphere and the disk can be observed.

In this chapter, we carry out an experimental study of the flow past a circular disk at high Reynolds with the motivation of searching for flow patterns that were found numerically by Gushchin and Matyushin (2006) in the analysis of the flow past a sphere at high Reynolds numbers. For Reynolds number in the range of $275 < Re < 375$ they found that about a plane can be observed in the wake behind the sphere. However, if the Reynolds number increases, being in the range of $375 \leq Re \leq 380$, the wake starts to rotate slowly around the plane of symmetry.
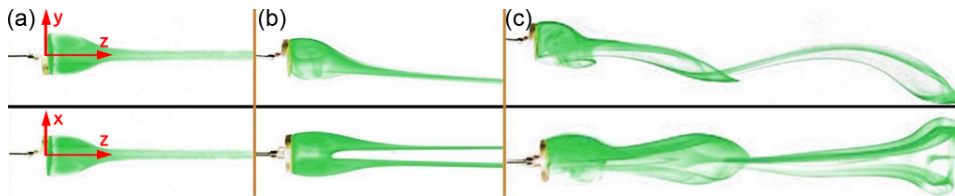

Figure 5.1: Visualization patterns of different regimes in the flow past a disk with $\frac{d}{h} = 6$. a) Steady axisymmetric flow (Re = 50). (b) Steady flow with planar symmetry (Re = 135). (c) Unsteady flow with hairpin shedding (Re = 180) (Bobinski et al., 2014).
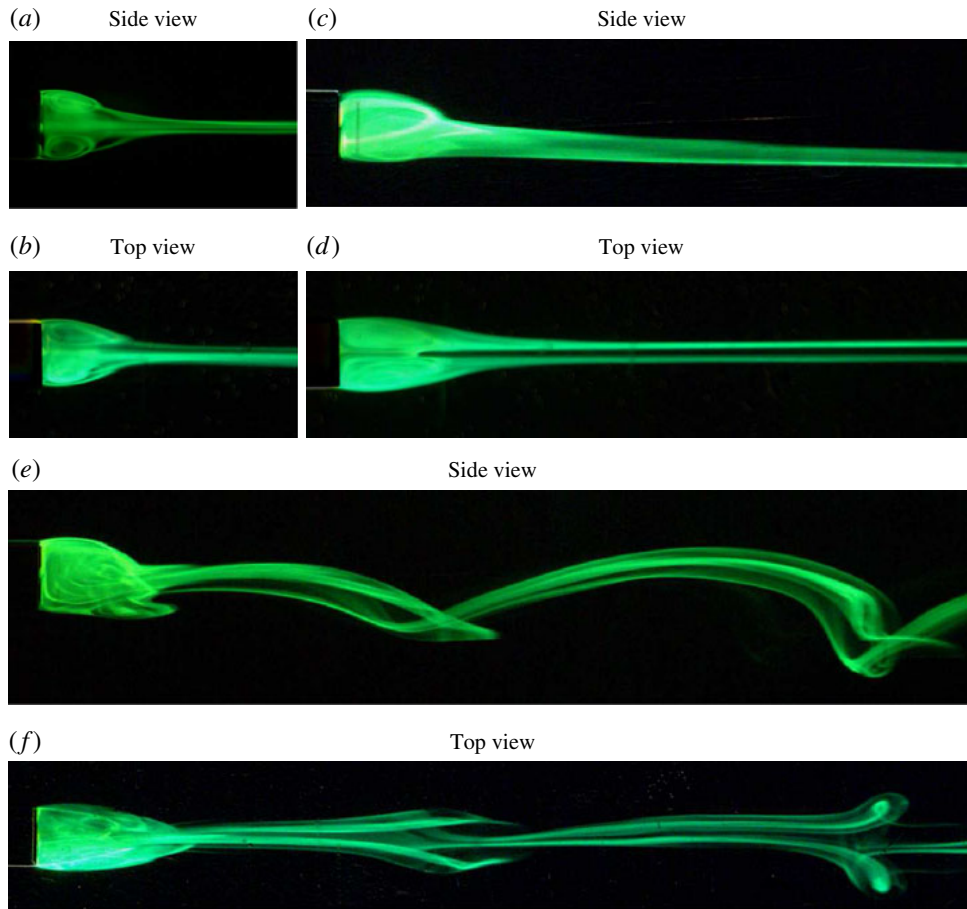
Figure 5.2: Visualization patterns of different regimes for the flow past a cube: a) and b) Basic flow at $Re = 100$, c) and d) Pattern with two counter-rotating vortices at $Re = 250$ and e) and f) hairpin vortex shedding regime at $Re = 300$ (Klotz et al., 2014).

5.2 Experimental setup.

The experimental setup, whose sketch is shown in figure 5.3, has been used previously for similar studies at low Reynolds numbers (Bobinski et al., 2014; Klotz et al., 2014; Thiria et al., 2006). It consists of a horizontal water channel with 860 mm in length and a cross-section viewing area of 100 mm × 100 mm. The flow is produced by a constant pressure gradient generated by gravity, using a tank located at a constant height above the channel. Two honeycomb type filters are used before the test zone. The flow velocity in the channel is controlled by means of two throttling valves. We used a disc with a diameter of $D = 20$ mm and a thickness of 3 mm, which gives us a blocking ratio of 0.12, i.e. the ratio of the diameter of the disc and the width of the channel. Water average speed range from 1.12 to 2.49 cm/s giving a Reynolds number in the range of 250< Re <550. The Reynolds number is defined as $Re = \frac{UD}{\nu}$ where U is the velocity of

free stream flow measured far from the obstacle, D is the diameter of the disk, and ν is the kinetic viscosity of the water. The disk is attached by a hollow capillary tube through which dye is injected for visualization. The particle image velocimetry (PIV) method was used to obtain quantitative measurements of the velocity field. It comprises a CCD camera that works at 14 Hz, a YAG double-pulsed laser, a timing box to synchronize the laser with the camera and an optical module to produce the laser sheet. Spheres of 11 μm diameter were used as tracers to perform the PIV. All PIV measurements were made in the rear view configuration, i.e. the laser sheet was perpendicular to the direction of the flow and located $x = 40$ mm downstream the obstacle.
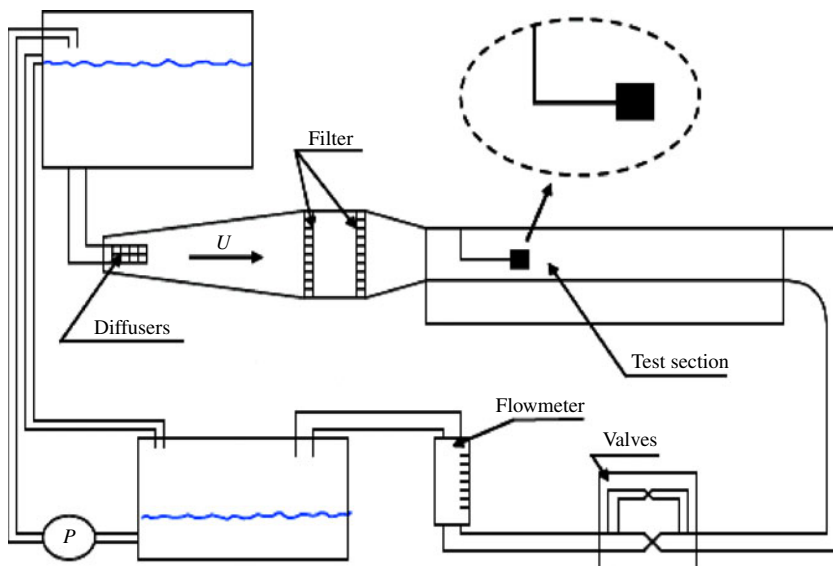
Figure 5.3: Experimental setup (Klotz et al., 2014).

5.3 Short term results

In this section, we present short term results of the vortex shedding for a flow past a disk at Re= 266 with the aim at comparing with the vorticity field that has been reported previously for this flow (Bobinski et al., 2014). The whole experiment in this section was observed along 50 seconds. Figure 5.4 shows the time evolution of the longitudinal vorticity fields for one period of the hairpin vortex obtained through PIV measurements taken at 14 Hz. The red color corresponds to positive vorticity and blue color to negative vorticity. It is found that our PIV measurements reproduce the results previously obtained by Bobinski et al. (2014) shown in figure 5.5.
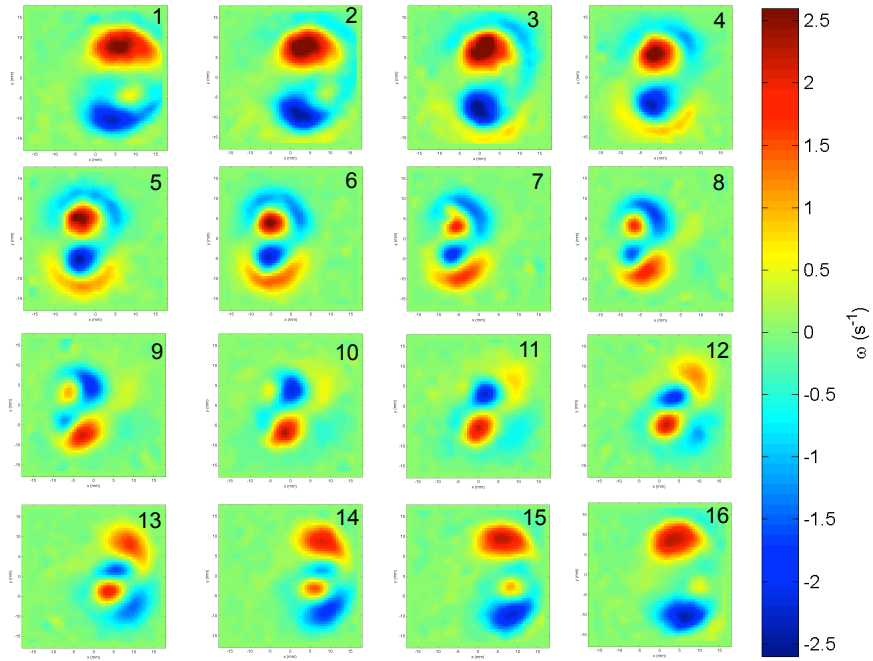
Figure 5.4: Experimental longitudinal vorticity fields for unsteady flow past a disk for one period of hairpin vortex shedding. $Re = 266$. $\frac{d}{h} = 2$. The time elapsed between two consecutive panels is 1/14 s.
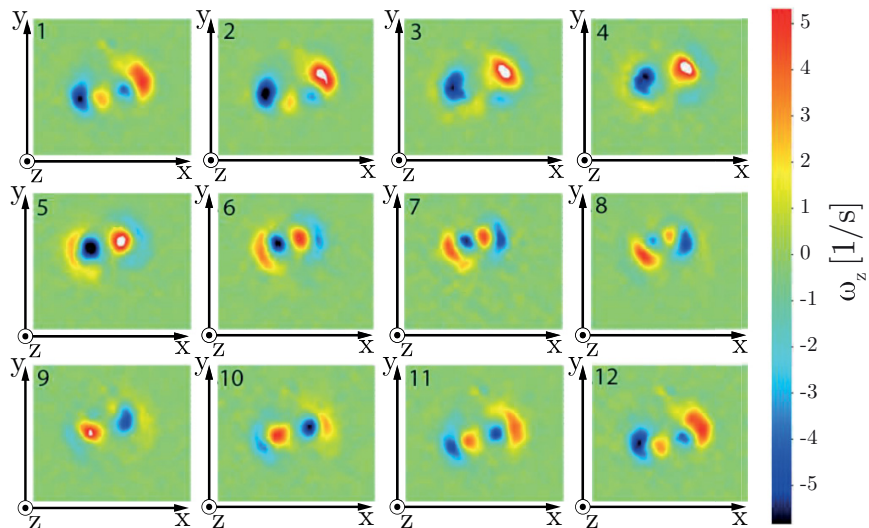

Figure 5.5: Experimental vorticity fields for unsteady flow past a disk for one period of hairpin shedding. $Re = 220$, $\frac{d}{h} = 24$. (Bobinski et al., 2014)

With the purpose of understanding the structure of the hairpin vortex flow pattern, figure 5.6 presents a side and top views of the visualized flow pattern (upper panels) and, four cross-sections of the corresponding vorticity field, marked with an arrow, obtained with PIV at different times (lower panels). The vorticity fields are numerated from right to left. In the field number 1 four vortices are observed, two internal vortices and two external vortices surrounding the internal ones. A dipole is observed in the center which is formed by a positive vortex (red color) that is above an imaginary horizontal symmetry axis and a negative vortex (blue color) that is below the horizontal symmetry axis. The external vortices have opposite vorticity sign with respect to the internal vortices, *i.e.*, the negative vortex is above the horizontal symmetry axis while the positive vortex is below this axis. As we move in the wake from right to left we observe that the external vortices tend to move towards the center, as observed in the vorticity field 2. In the vorticity field 3 four vortices appear again, two internal and two external but with opposite sign of vorticity with respect to those observed in the vorticity field 1. Finally, in the vorticity field 4 the external vortices tend to move towards the center as in the vorticity field 2 but with an opposite sign of vorticity.

In the previous explanation we considered a picture of the flow at a given time and analyzed different sections of the wake. It is worth remembering that in our experiment the laser sheet is fixed and the flow is the one that moves so that for our experiment the velocity fields correspond to different instants of time taken in the same position of the laser.
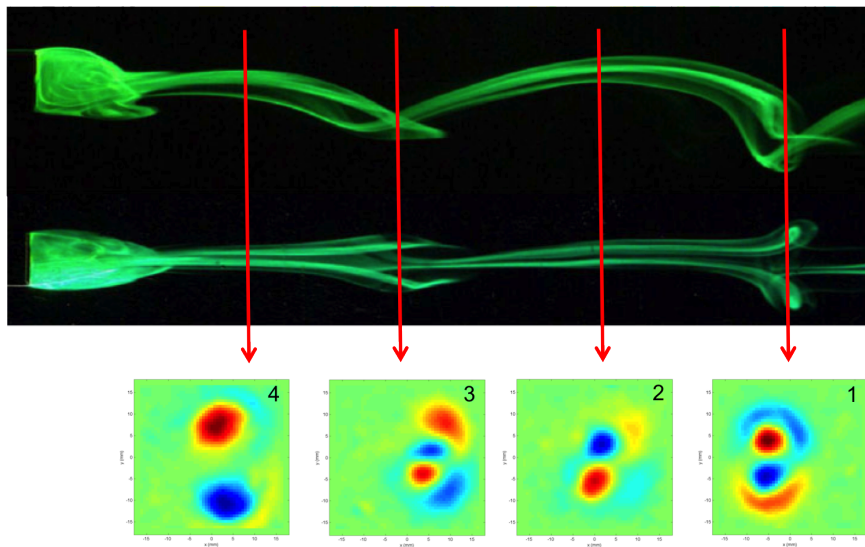

Figure 5.6: Upper panel: Hairpin vortex structure visualized from the side and top views. Lower panel: Vorticity fields of the wake cross-section obtained from PIV at different times.

In order to have a better understanding of the flow for Reynolds numbers where vortex detachment occurs, the group has implemented a MATLAB code to analyze the longitu-

dinal vorticity field by means of the azimuthal Fourier decomposition. In what follows, we offer a brief description of the algorithm(Bobinski et al., 2014).

First, the axial vorticity, ω_z, in cartesian coordinates is transformed to a mesh in polar coordinates. In this way, ω_z is expressed as discrete arrays that are functions of the radius r_j and the angle θ_n. After that, azimuthal Fourier transformation was performed in one direction

$$\hat{\omega}^{azim}(r_j, m) = \sum_n \omega_z(r_j, \theta_n) exp(-im\theta_n), \tag{5.1}$$

and later integrated in radial direction.

$$\hat{\omega}_m = \sum_j \hat{\omega}^{azim}(r_j, m) r_j \delta r, \tag{5.2}$$

obtaining the azimuthal modal coefficients of the longitudinal vorticity.

Using the MATLAB code, we analyzed the results obtained with the PIV technique. In figure 5.7 the comparison between the original vorticity field and the results obtained by azimuthal Fourier decomposition, is presented. A good agreement between the original longitudinal vorticity field and the sum of the modes obtained by the azimuth Fourier decomposition is observed. We also observe the decomposition of the instantaneous vorticity fields for the first 6 modes and the sum of the modes without considering the mode 0. We notice that the figure with the sum of modes without mode 0 reproduces quite well the original vorticity field. Mode 1 and mode 2 are the most influential modes in the flow, as we can observe in the value of the vorticity of these modes. Note that the values of the mode 1 are an order of magnitude greater than the rest of the modes .
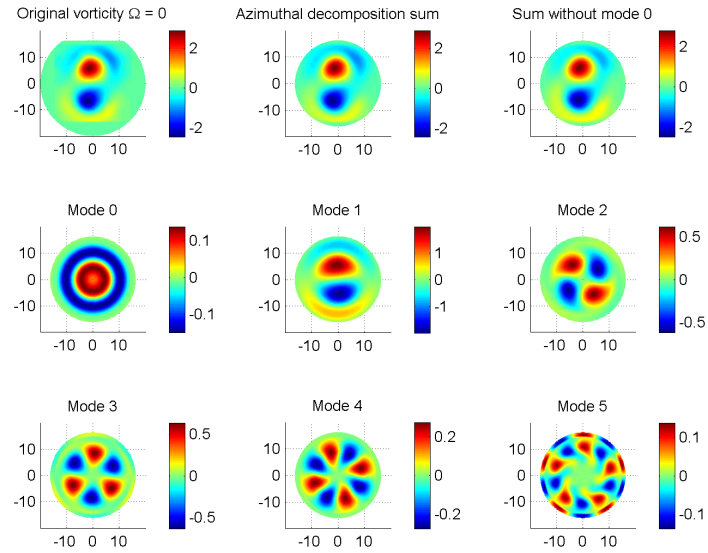
s

Figure 5.7: Azimuthal Fourier decomposition of vorticity fields: In the upper left corner the field obtained directly from the PIV is presented. In the first row, the central panel corresponds to the sum of the modes obtained from the azimuthal decomposition. In the upper right corner, the sum of the modes minus the zero mode is presented. The rest of the figures corresponds to the indicated modes. $Re = 266$.
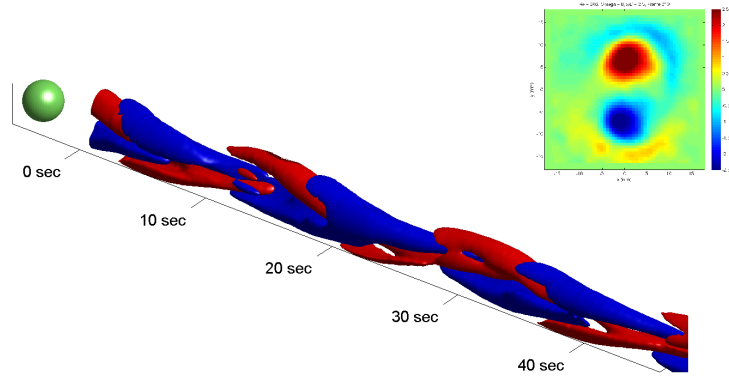
Figure 5.8: Temporal evolution of the longitudinal component of the vorticity, ω_z, calculated from the velocity measured in the laser plane located normally to the free-stream velocity. $Re = 266$. Sum of modes 0, 1, and 2.
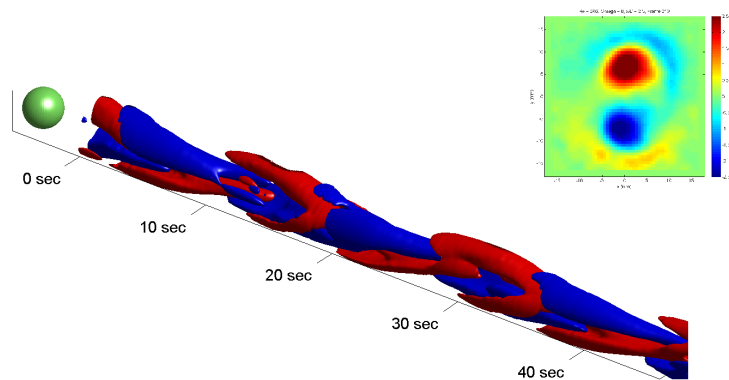

Figure 5.9: Temporal evolution of the longitudinal component of the vorticity, ω_z, calculated from the velocity measured in the laser plane located normally to the free-stream velocity. $Re = 266$. Sum of modes 1 and 2.

Finally, we present figures of the temporal evolution of the longitudinal component of the vorticity, ω_z. If we compare the figures of the sum of the modes against the sum of the modes without mode 0, namely , figures 5.8 and 5.9 respectively, we observe that there is no appreciable difference between them so we conclude that Mode 0 does not introduce a clear modification in the behavior of the flow.
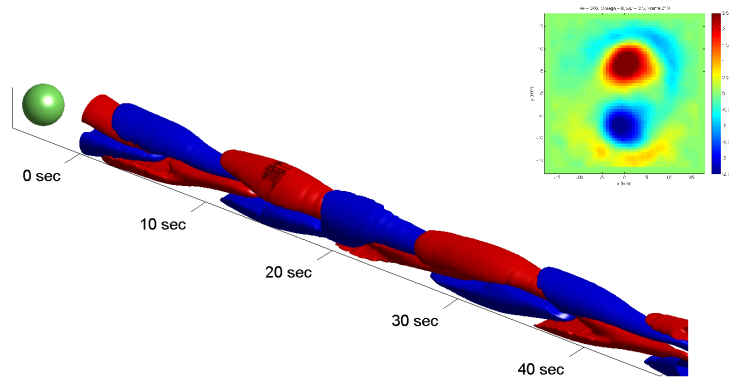

Figure 5.10: Temporal evolution of the longitudinal component of the vorticity, ω_z, calculated from the velocity measured in the laser plane positioned normally to the free-stream velocity. $Re = 266$. Mode 1.

In the figure 5.10 the temporal evolution for the mode 1 of the longitudinal vorticity is shown. Notice the alternation in the sign of vorticity for two and a half periods of the hairpin vortex.

5.4   Long term results for $250 \leq \mathrm{Re} \leq 550$

In order to make a better flow analysis it was necessary to have a larger sample in time. Therefore, for the results we present hereafter, the data acquisition was obtained with a frequency of 2 Hz. The experiments presented in this section consisted of increasing the Reynolds number and analyzing the results as in the case presented previously. Experimental Reynolds numbers in the range $250 < Re < 550$ were varied with increments of 50. Figure 5.11 shows the time-dependent vorticity fields for one period of the hairpin vortex shedding and Re = 250. Unlike the results shown for $Re = 266$ these results have not been subject to a post processing so the image quality is not as good as in the previous

results, however it is possible to see in the vorticity field number 3 the four vortices, two internal and two external, as those shown in the previous section. This structure can also be appreciated in the vorticity field number 9 but the sign of the vorticity is inverted with respect to the vorticity field number 3.
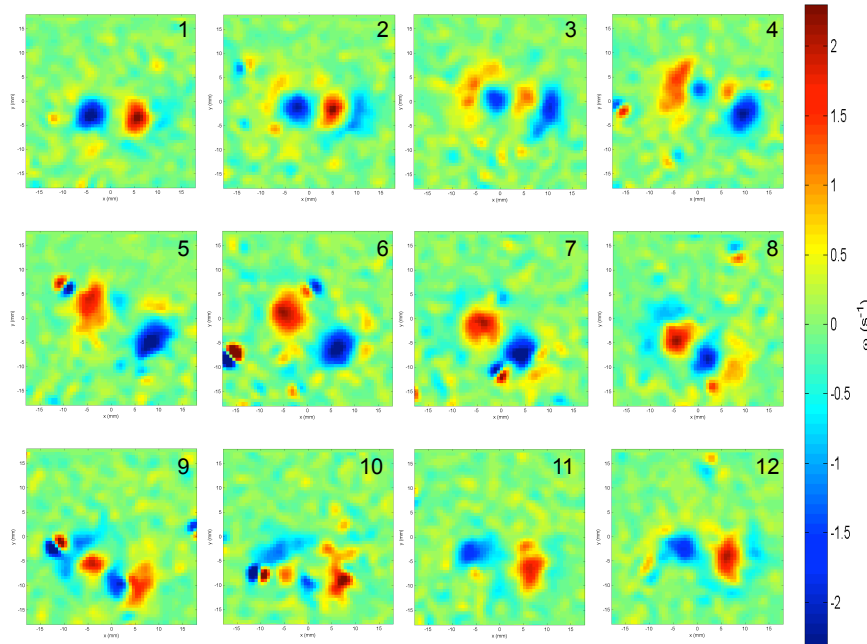

Figure 5.11: Vorticity fields for the unsteady flow past a disk for one period of the hairpin vortex shedding. Re = 250.

Figures 5.12 and 5.13 show the time-dependent vorticity fields for one period of the hairpin vortex shedding with $Re = 350$. The figures correspond to the same experiment but at different time intervals. In figure 5.12, the vorticity field number 9 shows the structure of the hairpin vortex characterized by the pair of internal vortices surrounded by two external vortices. After time, we observe that the external vortices move towards the central region. Figure 5.13 shows also a pattern of four vortices, two internal and two external but now we can notice a rotation in the symmetry axis. In order to appreciate this rotation more clearly, in figure 5.14 two vorticity fields of the same experiment taken at different times are shown, where a dotted line is drawn to serve as an axis to illustrate the rotation. It is clearly observed that there is a 90 degrees rotation of the hairpin vortex structure.
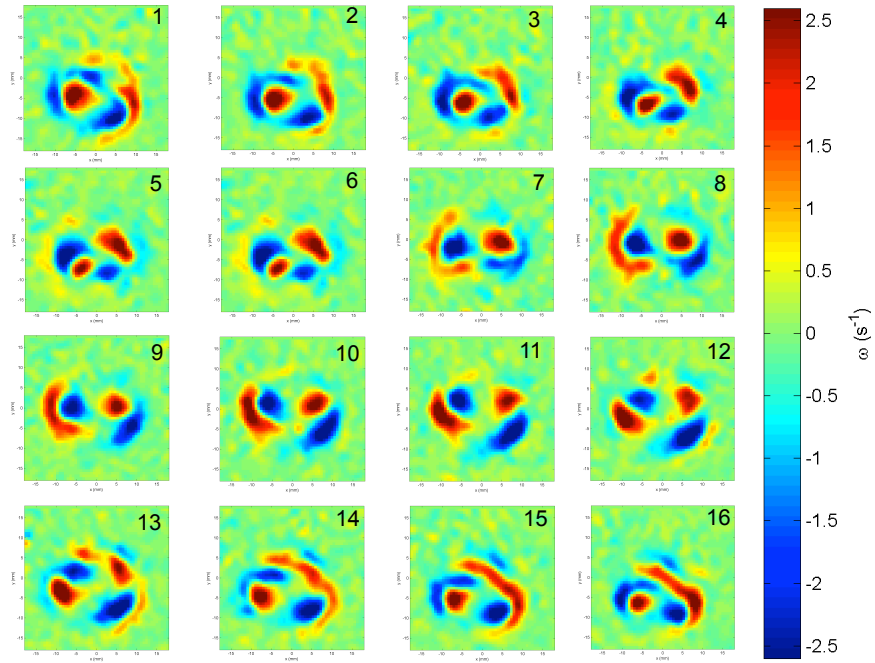
Figure 5.12: Vorticity fields for the unsteady flow past a disk for one period of the hairpin vortex shedding. Re = 350. Time interval: $t = 5 - 12s$.
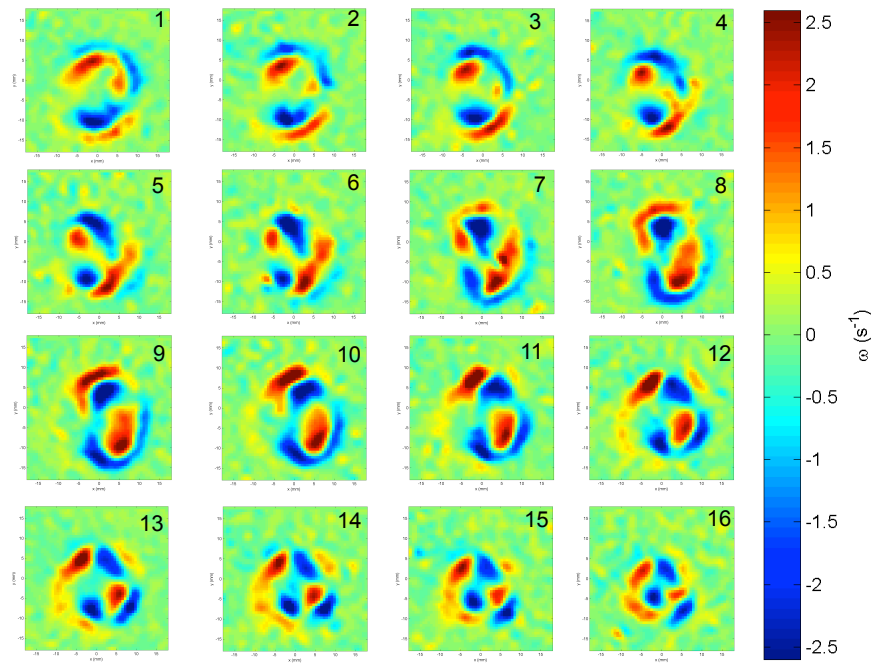

Figure 5.13: Vorticity fields for the unsteady flow past a disk for one period of the hairpin vortex shedding. Re = 350. Time interval:$t = 49 - 56s$.
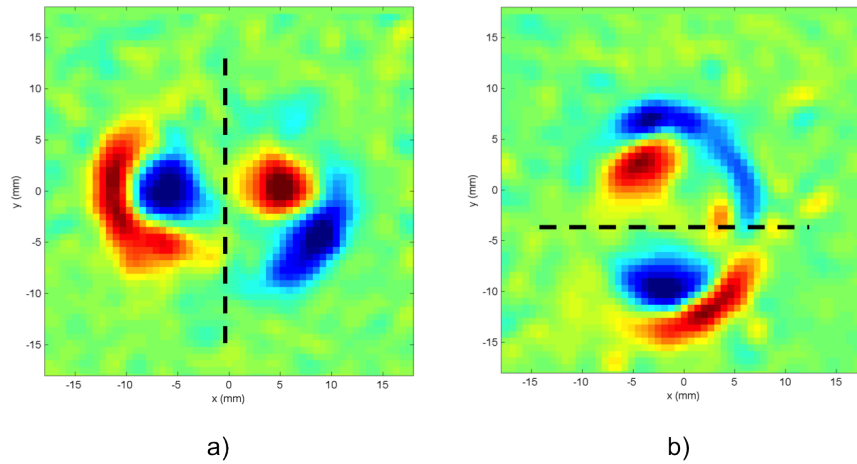
a)   b)

Figure 5.14: Vorticity fields for the unsteady flow past a disk at two time instants of the hairpin vortex shedding. Re $= 350$. a)$t = 8s$ y b) $t = 50s$.

Finally, figures 5.15 and 5.16 present the temporal evolution of longitudinal vorticity, ω_z, for $Re = 250$ and $Re = 350$, respectively. In figure 5.15 the alternation between negative and positive vorticity is observed along 172 seconds. In figure 5.16 the rotation of the vortex is not observed so clearly, and a change in the behavior of the structure can be observed at 70 and 140 seconds, which seems to indicate that there is a hidden frequency in the phenomenon that requires measurements over longer time to explore if this alteration is repeated.
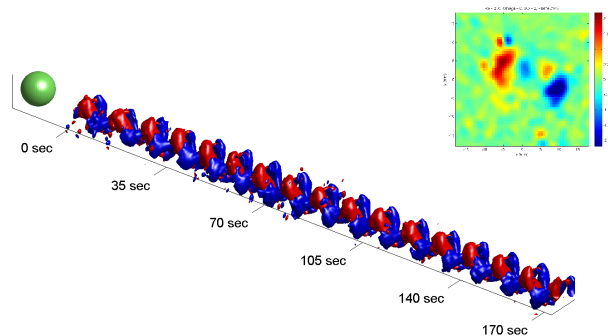

Figure 5.15: Temporal evolution of the longitudinal component of the vorticity, ω_z, calculated from the velocity measured in the laser plane positioned normally to the free-stream velocity. $Re = 250$.
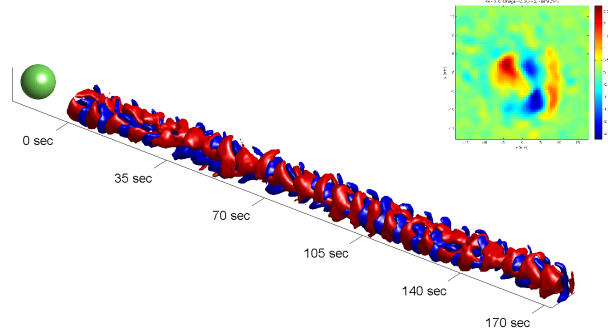
Figure 5.16: Temporal evolution of the longitudinal component of the vorticity, ω_z, calculated from the velocity measured in the laser plane positioned normally to the free-stream velocity. $Re = 350$.

5.5 Conclusions.

In this Chapter, we have present experimental results performed during a research stay at the facilities of the PMMH-EPSCI (Physique et Mécanique des Milieux Hétérogènes-Ecole de Physique et de Chimie Industrielles) of ParisTech in Paris, France. The flow past a circular disk immersed completely in a water channel was studied varying the Reynolds numbers in the range of $250 \leq Re \leq 550$. From PIV measurements taken in the rear view configuration, the longitudinal vorticity field was obtained as a function of time. To get a better understanding of the flow pattern, the temporal evolution of the longitudinal vorticity was analyzed using an azimuthal Fourier decomposition. For high Reynolds numbers, results show a rotation of the symmetry axis of the characteristic flow pattern, known as hairpin vortex. Results obtained so far are not concluding, therefore, long-term experiments are needed to determine the possible existence of hidden frequencies. The question remains whether the hairpin vortex present a complete rotation for which a further analysis is required in order to find a definitive answer.

Conclusions

This thesis was devoted to the experimental and numerical study of wake patterns created by localized Lorentz forces acting as (magnetic) obstacles in flows of an electrically conducting fluid either an electrolyte or a liquid metal. An additional case of the wake created by the flow past a solid circular disk was also analyzed. The knowledge of wake patterns is relevant in multiple interesting problems such as animal locomotion, vehicle design, wind energy devices, structure design, heat transfer enhancement, and many others. To deepen the knowledge of this topic, laboratory experiments and numerical simulations are indispensable. In this context, the use of localized electromagnetic forces in conducting fluids provides an alternative for the controlled generation of wake patterns in laboratory, and makes it possible to study a wider variety of physical behaviors than those found in the flow past solid obstacles.

First, it was presented the study of the wake generated in the flow created by a traveling localized Lorentz force in an electrolyte layer. The flow was analyzed experimentally and the results were compared with numerical solutions obtained by a Q2D code. Different flow patterns were identified as the dimensionless parameters controlling the flow were varied. The results showed the presence of a 2P wake pattern and the transition to the BvK wake by increasing the Reynolds number. Through measurement of the kinetic energy in the wake it was shown that by increasing Re, the inertia force overcomes the electromagnetic braking force .

Additionally, the flow past a pair of magnetic obstacles side by side in an electrolyte layer at a fixed Reynolds number was studied numerically. We analyzed the interaction of the wakes created behind the obstacles for different values of the dimensionless separation distance. The results presented similar regimes as those observed in the wakes created by a pair of solid cylinders, including the bistable regime. In order to have a more complete understanding, it is necessary to explore the flow at different Reynolds numbers, for example, it would be of interest to observe the coupling of 2P wakes since these may be relevant for heat transfer enhancement applications. In addition, it is required to obtain experimental results that can be used to validate the developed numerical models. With the experimental equipment presented in this work, these results could easily be obtained

The wall effect on wake patterns generated in the flow past a magnetic obstacle in a narrow channel was also explored by varying the Reynolds number, the Lorentz force parameter and the blockage parameter. Results revealed that as the blockage parameter increase, the flow recovers stability. Results were presented in condensed form through transition maps obtained both experimentally and with numerical simulations using a Q2D code.

69

Simulations show a good agreement with the experimental results. It is worth mentioning that, contrary to what happened in the case of wakes past solid obstacles, the wake past a magnetic obstacle may become unstable for values of $Re = 100$ and $\beta = 1/2$ because there is an additional governing parameter, namely, the Lorentz force parameter, through which the braking force can be modulated.

In addition, an experimental and theoretical study of the liquid metal flow past a magnetic obstacle was carried out. The flow was characterized through the measurement of the longitudinal velocity component by Ultrasound Doppler Velocimetry (UDV). It was found that the energy of the perturbations in the wake that characterize the vortex shedding behind the magnetic obstacle increases with the Reynolds number to reach a maximum that depends on the Hartmann number. Then the energy reduces monotonically up to the maximum Reynolds number reached in the experiment. This indicates that the oscillatory wake is present in the liquid metal flow only in a finite range of Reynolds numbers. This behavior is completely different from the observed in the flow past a solid obstacle.

Finally, some experimental results obtained in the flow past a solid circular disk immersed in a water channel were presented. The experiments were carried out for high Reynolds numbers ($250 \leq Re \leq 550$). Using PIV measurements, longitudinal vorticity fields were obtained. The hairpin vortex flow pattern was found at Re=250. Interestingly, for Re=350 the structure of the hairpin vortices presented a rotation in the symmetry axis although it is still necessary a deeper study to fully characterize this observation. In order to obtain more information of the flow, the temporal evolution of the longitudinal vorticity component was analyzed. Results seem to indicate the presence of a hidden frequency, however, it is necessary to carry out long-term experiments to determine it. These experiments were performed at the facilities of the PMMH-EPSCI (Physique et Mécanique des Milieux Hétérogènes-École de Physique et de Chimie Industrielles) of ParisTech in Paris, France, during a research stay and it is planned to continue this collaboration to complete the study.

The experimental and numerical study carried out in this thesis is expected to contribute to a better understanding of the flow past a magnetic obstacle and to motivate the application of the generated knowledge in technological devices, particularly, for heat transfer enhancement. The experimental data will also be a valuable information for the validation and improvement of computational tools.

Bibliography

Afanasyev, D. and Korabel, V. N. (2006*a*), 'Wakes and vortex streets behind a localized force: Numerical simulations', *Communications in Nonlinear Science and Numerical Simulations* **13**, 1101–1111.

Afanasyev, Y. D. (2006), 'Formation of vortex dipoles', *Phys. Fluids* **18**, 037103.

Afanasyev, Y. D. and Deacon, C. G. (2006), 'Investigating vortex streets behind real and virtual bluff bodies', *Am. J. Phys.* **74**, 236–239.

Afanasyev, Y. D. and Korabel, V. N. (2006*b*), 'Wakes and vortex streets generated by translating force and force doublet: laboratory experiments', *J. Fluid Mech.* **553**, 119–141.

Alcalá, G. and Cuevas, S. (2014), 'Surface waves generated on electrolytes by a traveling electromagnetic force.', *J. Klapp and A. Medina (Eds.) Experimental and Computational Fluid Mechanics. Springer, 2014.* .

Allen, J. J. and Smith, A. J. (2001), 'Energy harvesting eel.', *Journal of fluids and structures* **15(3-4)**, 629–640.

Andreev, O., Kolesnikov, Y. and Thess, A. (2009), 'Application of the ultrasonic velocity profile method to the mapping of liquid metal flows under the influence of a non-uniform magnetic field.', *Exp. Fluids* **49**, 77–83.

Beltrán, A. (2010), Flow dynamics in magnetic obstacles, PhD thesis, National Autonomous University of Mexico.

Bobinski, T., Goujon-Durand, S. and Wesfreid, J. (2014), 'Instabilities in the wake of a circular disk..', *Phys. Rev. E* **89(5)**, 053021.

Camarri, S. and Giannetti, F. (2007), 'On the inversion of the von karman street in the wake of a confined square cylinder', *J. Fluid Mech.* **574**, 169–178.

Cruz, F. S., Martínez, S. M., Elizondo, J. C., no B., A. F. P., noz, A. G. M., Ávila, J. R. and Armas, V. O. (2010), 'Estudio experimental de la generación de vórtices en salmuera por mhd'.

Cuevas, S., Smolentsev, S. and Abdou, M. (2006*a*), 'On the flow past a magnetic obstacle.', *J. Fluid Mech.* **553**, 227–252.

Cuevas, S., Smolentsev, S. and Abdou, M. (2006*b*), 'Vorticity generation in the creeping flow past a magnetic obstacle', *Phys. Rev. E* **74**, 056301–1–056301–10.

Davis, R. W., Moore, E. F. and Purtell, L. P. (1984), 'A numerical experimental study of confined flow around rectangular cylinders', *Phys. Fluids* **27(1)**, 46–59.

Domínguez, D. R., Beltrán, A., Román, J., Cuevas, S. and Ramos, E. (2015), 'Experimental and theoretical study of the dynamics of wakes generated by magnetic obstacles.', *Magnetohydrodynamics* **51**, 215 – 224.

Duran-Matute, M., Trieling, R. R. and van Heijst, G. J. F. (2011), 'Scaling and asymmetry in an electromagnetically forced dipolar flow structure.', *Phys. Rev. E* **83**, 016306.

Fiebig, M. (1997), 'Vortices and heat transfer.', *ZAMM Journal of Applied Mathematics and Mechanics/Zeitschrift für Angewandte Mathematik und Mechanik* **77(1)**, 3–18.

Figueroa, A. (2010), Dynamics of vortices generated by electromagnetic forces, PhD thesis, National Autonomous University of Mexico.

Figueroa, A., Cuevas, S. and Ramos, E. (2011), 'Electromagnetically driven oscillatory shallow layer flow', *Phys. Fluids* **23**, 013601.

Figueroa, A., Demiaux, F., Cuevas, S. and Ramos, E. (2009), 'Electrically driven vortices in a weak dipolar magnetic field in a shallow electrolytic layer', *J. Fluid Mech.* **641**, 245–261.

Gelfgat, Y. and Olshanskii, S. V. (1978), 'Velocity structure of flows in non-uniform constant magnetic fields ii. experimental results.', *Magnetohydrodynamics.* **14(2)**, 151–154.

Gelfgat, Y., Peterson, D. and Shcherbinin, E. V. (1978), 'Velocity structure of flows in non-uniform constant magnetic fields 1. numerical calculations.', *Magnetohydrodynamics.* **14(1)**, 55–61.

Godoy-Diana, R., Aider, J. L. and Wesfreid, J. E. (2008), 'Transitions in the wake of a flapping foil.', *Phys. Rev. E* **77(1)**, 016308.

Griebel, M., Dornseifer, T. and Neunhoeffer, T. (1998), *Numerical Simulation in Fluid Dynamics*, SIAM.

Gumowski, K., Miedzik, J., Goujon-Durand, S., Jenffer, P. and Wesfreid, J. (2008), 'Transition to a time-dependent state of fluid flow in the wake of a sphere.', *Phys. Rev. E* **77(5)**, 055308.

Gushchin, V. and Matyushin, R. V. (2006), 'Vortex formation mechanisms in the wake behind a sphere for 200¡ re¡ 380.', *Fluid Dynamics* **41(5)**, 795–809.

Heinicke, C. (2013), 'Spatially resolved measurements in liquid metal flow with lorentz force velocimetry.', *Exp. Fluids* **54(6)**, 18.

Honji, H. (1991), 'Wavy wake formation in the absence of submerged bodies in electrolyzed salt water..', *J. Phys. Soc. Japan* **60**, 1161–1164.

Honji, H. and Haraguchi, Y. (1995), 'Electrolytically induced quasi-two-dimensional vortex pairs.', *J. Phys. Soc. Japan* **64**, 2274–2277.

Ikehata, Y., Honji, H. and Sugihara, Y. (1996), 'Formation of periodic vortex streets driven by the lorentz force', *Engineering Sciences Reports, Kyushu University* **17**, 437–442.

Irwin, P. (Sept. 2010), 'Vortices and tall buildings: a recipe for resonance.', *Phys. Today* pp. 68 – 69.

Jian, D. and Karcher, C. (2012), 'Electromagnetic flow measurements in liquid metals using time-of-flight lorentz force velocimetry.', *Meas. Sci. Tech* **23(7)**, 074021.

Kenjeres, S. (2012), 'Energy spectra and turbulence generation in the wake of magnetic obstacles', *Phys. Fluids* **24**, 115111.

Kenjeres, S., ten Cate, S. and Voesenek, C. (2011), 'Vortical structures and turbulent bursts behind magnetic obstacles in transitional flow regimes', *Int. J. Heat and Fluid Flow* **32**, 510–528.

Klotz, L., Goujon-Durand, S., Rokicki, J. and Wesfreid, J. (2014), 'Experimental investigation of flow behind a cube for moderate reynolds numbers.', *J. Fluid Mech.* **750**, 73–98.

Le Gal, P., Chauve, M., Lima, R. and Rezende, J. (1990), 'Couple wakes behind two circular cylinders.', *Phys. Rev. A* **41**, 4566–4569.

Le Gal, P., Peschard, I., Chauve, M. and Takedaa, Y. (1996), 'Collective behavior of wakes downstream a row of cylinders', *Phys. Fluids* **8**, 2097–2106.

Lynch, S. (2004), *Dynamical Systems whit applications using Matlab.*, Birkhauser, Boston.

McCaig, M. (1977), *Permanent Magnets in Theory and Practice*, Wiley.

Moin, P. and Kim, J. (January. 1997), 'Tackling turbulence with supercomputers.', *Sci. Am.* pp. 62 – 68.

Peschard, I. and Le Gal, P. (1996), 'Coupled wakes of cylinders.', *Phys. Rev. Lett.* **77**, 3122–3125.

Prinz, S., Bandaru, V., Kolesnikov, Y., Krasnov, D. and Boeck, T. (2016), 'Numerical simulations of magnetohydrodynamic flows driven by a moving permanent magnet.', *Phys. Rev. Fluids.* **1**, 043601.

Ramos, E., Beltrán, A., Cuevas, S. and Smolentsev, S. (2008), 'Dynamic properties of a magnetic obstacle.', *In: Book of Abstracts of the 7th International PAMIR Conference. Presquíle de Giens, France* **2**, 891–895.

Rehimi, F., Aloui, F., Nasrallah, S. B., Doubliez, L. and Legrand, J. (2008), 'Experimental investigation of a confined flow downstream of a circular cylinder centred between two parallel walls.', *Journal of Fluids and structures* **24 (6)**, 855–882.

Román, J. (2013), Estudio numérico de la transferencia de calor en un flujo a través de arreglos de obstáculos magnéticos, Master's thesis, National Autonomous University of Mexico.

Román, J., Beltrán, A. and Cuevas, S. (2015), 'Numerical simulation of the flow past a pair of magnetic obstacles.', *J. Klapp and A. Medina (Eds.) Experimental and Computational Fluid Mechanics. Springer, 2014.* .

Román, J., Figueroa, A. and Cuevas, S. (2017), 'Experimental and theoretical study of the dynamics of wakes generated by magnetic obstacles.', *Magnetohydrodynamics* **53**, 55 – 66.

Samsami, F., Kolesnikov, Y. and Thess, A. (2014), 'Vortex dynamics in the wake of a magnetic obstacle.', *J. Vis.* **17**, 245–252.

Schnipper, T., Andersen, A. and Bohr, T. (2009), 'Vortex wakes of a flapping foil..', *J. Fluid Mech.* **633**, 411–423.

Singha, S. and Sinhamahapatra, K. P. (2010), 'Flow past a circular cylinder between parallel walls at low reynolds numbers', *J. Ocean Eng.* **37**, 757–769.

Sumner, D., Wong, S., Price, S. J. and Paidoussis, M. (1999), 'Flow behavior of side-by-side circular cylinders in steady cross-flow..', *J. Fluids and Structures* **13**, 309–338.

Thielicke, W. and Stamhuis, E. (2014), 'Pivlab-towards user-friendly, affordable and accurate digital particle image velocimetry in matlab.', *J. Open Res. Software* **2(1)**.

Thiria, B., Goujon-Durand, S. and Wesfreid, J. (2006), 'The wake of a cylinder performing rotary oscillations..', *J. Fluid Mech.* **560**, 123–147.

Tympel, S., Boeck, T. and Schumacher, J. (2013), 'Laminar and transitional liquid metal duct flow near a magnetic point dipole', *J. Fluid Mech.* **735**, 553–586.

Versteeg, H. and Malalasekera, W. (1995), *An Introduction to Computational Fluid Dynamics: The Finite Volume Method.*, Longman Scientific and Technical.

Votyakov, E., Kolesnikov, Y., Andreev, O., Zienicke, E. and Thess, A. (2007), 'Structure of the wake of a magnetic obstacle.', *Phys. Rev. Lett.* **98**, 144504.

Votyakov, E. V. and Kassinos, S. C. (2009), 'On the analogy between streamlined magnetic and solid obstacles.', *Phys. Fluids* **21(9)**, 097102.

Votyakov, E. V. and Kassinos, S. C. (2010), 'Core of the magnetic obstacle.', *J. Turbulence* **11(49**, 1–15.

Votyakov, E., Zienicke, E. and Kolesnikov, Y. (2008), 'Constrained flow around a magnetic obstacle.', *J. Fluid Mech.* **610**, 131 – 156.

Wang, X. and Alben, S. (2015), 'The dynamics of vortex streets in channels', *Phys. Fluids* **27**, 073603.

Williamson, C. H. K. (1996), 'Vortex dynamics in the cylinder wake.', *Annual Review of Fluid Mechanics* **28**, 477–539.

Zdravkovich, M. M. (1985), 'Flow induced oscillations of two interfering circular cylinders.', *J. of Sound and Vibration* **101**, 511–521.

Zdravkovich, M. M. (1997), *Flow around circular cylinders, vol I.*, Oxforf University Press.

Zhang, X. and Huang, H. (2013), 'Effect of local magnetic fields on flow and heat transfer', *ASME J. Heat Transfer* **135**, 021702.